



## Exploring the environment, magnetic fields, and feedback effects of massive high-redshift galaxies with [CII]

Downloaded from: <https://research.chalmers.se>, 2025-07-02 11:09 UTC

Citation for the original published paper (version of record):

Kade, K., Knudsen, K., Vlemmings, W. et al (2023). Exploring the environment, magnetic fields, and feedback effects of massive high-redshift galaxies with [CII]. *Astronomy and Astrophysics*, 673.  
<http://dx.doi.org/10.1051/0004-6361/202141839>

N.B. When citing this work, cite the original published paper.

# Exploring the environment, magnetic fields, and feedback effects of massive high-redshift galaxies with [C II]

K. Kade<sup>1</sup>, K. K. Knudsen<sup>1</sup>, W. Vlemmings<sup>1</sup>, F. Stanley<sup>2</sup>, B. Gullberg<sup>3</sup>, and S. König<sup>1</sup>

<sup>1</sup> Department of Space, Earth, & Environment, Chalmers University of Technology, Chalmersplatsen 4 412 96 Gothenburg, Sweden  
e-mail: [kiana.kade@chalmers.se](mailto:kiana.kade@chalmers.se)

<sup>2</sup> Institut de Radioastronomie Millimétrique (IRAM), 300 rue de la Piscine, 38400 Saint-Martin-d'Hères, France

<sup>3</sup> Cosmic Dawn Center DTU Space, Technical University of Denmark, Elektrovej 327, 2800 Kgs. Lyngby, Denmark

Received 21 July 2021 / Accepted 25 February 2023

## ABSTRACT

**Context.** Massive galaxies are expected to grow through different transformative evolutionary phases. High-redshift starburst galaxies and quasars are thought to be such phases and thus provide insight into galaxy evolution. Several physical mechanisms are predicted to play an important role in driving these phases; for example, interaction with companion galaxies, active galactic nuclei feedback, and possibly magnetic fields.

**Aims.** Our aim is to characterize the physical properties and the environment of the submillimeter galaxy AzTEC-3 at  $z = 5.3$  and the lensed quasar BRI 0952–0115 at  $z = 4.4$ , and to set a limit on the polarization properties of the two sources. We intend to place these two sources in the broader context of galaxy evolution, specifically star formation and mass growth through cosmic time.

**Methods.** We used full polarization, sub-arcsecond-resolution, ALMA band-7 observations of both BRI 0952–0115 and AzTEC-3. We detect [C II] ( $^2P_{3/2} - ^2P_{1/2}$ ) line emission towards both BRI 0952–0115 and AzTEC-3, along with companions in each field. We present an updated gravitational lensing model for BRI 0952–0115 for correction of gravitational magnification.

**Results.** We present infrared luminosities, star-formation rates, and [C II] line to infrared luminosity ratios for each source. The [C II] emission line profile for both BRI 0952–0115 and AzTEC-3 exhibit a broad, complex morphology, indicating the possible presence of outflows. We present evidence of a “gas bridge” between AzTEC-3 and a companion source. Modified blackbody spectral energy distribution fitting is used to analyze the properties of [C II] detected companion sources in the field of both the submillimeter galaxy and the quasar. We investigated the possible role of the detected companions in outflow signatures. Using a simple dynamical mass estimate for the sources, we suggest that both systems are undergoing minor or major mergers. No polarization is detected for the [C II], placing an upper limit below that of theoretical predictions.

**Conclusions.** Our results show that high-velocity wings are detected, indicating possible signs of massive outflows; however, the presence of companion galaxies can affect the final interpretation. Furthermore, the results provide additional evidence in support of the hypothesis that massive galaxies form in overdense regions, growing through minor or major mergers with companion sources. Finally, strong, ordered magnetic fields are unlikely to exist at the kiloparsec scale in the two studied sources.

**Key words.** galaxies: high-redshift – galaxies: evolution – galaxies: starburst – galaxies: ISM – galaxies: interactions – galaxies: magnetic fields

## 1. Introduction

The discovery of intense starbursts ( $100\text{--}1000 M_{\odot}$ ) at high redshift demonstrates the prevalence of short, transformative phases in the evolution of massive galaxies (e.g., [Smail et al. 1997](#); [Hughes et al. 1998](#); [Blain et al. 1999](#); [Casey et al. 2014](#)). Furthermore, the discovery of the relation between the mass of super-massive black holes (SMBHs) in the center of local massive galaxies and the velocity dispersion of those galaxies suggests coeval evolution between the SMBH and the host galaxy (e.g., [Magorrian et al. 1998](#); [Ferrarese & Merritt 2000](#); [Gebhardt et al. 2000](#); [Häring & Rix 2004](#); [Gültekin et al. 2009](#); [Beifiori et al. 2012](#); [Kormendy & Ho 2013](#); [Bennert et al. 2015](#); [Reines & Volonteri 2015](#)). The cosmic black hole accretion rate density has been found to follow a similar trend with redshift to that of the cosmic star-formation rate (SFR) density, indicating that a significant part of the evolution takes place during the first few billion years after the big bang (e.g., [Kormendy & Ho 2013](#); [Madau & Dickinson 2014](#)). Thus, characterizing the physical properties of high-redshift starburst galaxies and quasars is

essential for establishing a complete and coherent description of the evolution of massive galaxies.

Many physical mechanisms play a role in massive galaxy evolution. Galaxies are thought to grow through two main mechanisms, namely galaxy mergers and gas accretion from the intergalactic medium (e.g., [Kereš et al. 2005](#); [Hopkins et al. 2008](#); [Dekel et al. 2009](#); [Genzel et al. 2010](#); [Krumholz & Dekel 2010](#); [Di Matteo et al. 2012](#); [Dubois et al. 2012](#)). Additionally, the presence of a growing SMBH, as seen in active galactic nuclei (AGNs) and quasars has been found in theoretical modeling to provide a mechanism for regulating star formation (e.g., [Di Matteo et al. 2005](#); [Narayanan et al. 2015](#); [Harrison 2017](#)). This implies that characterizing the environment of high-redshift quasars and starbursts, as well as understanding the role of AGN feedback, is paramount to understanding the manner in which these galaxies evolve.

Simulations and theoretical predictions from the early universe have demonstrated the likelihood of ubiquitous major and minor mergers occurring at high redshift (e.g., [Kaviraj et al. 2013, 2015](#); [Fogasy et al. 2017](#)). Cosmological hydrodynamical

simulations such as Illustris (Sijacki et al. 2015) and Horizon-AGN (Dubois et al. 2014) can shed light on the effects of these interactions. Studies have shown that minor mergers (classified as those with mass-ratios of  $>1:4$ ) and the effect of companion galaxy interactions systematically affect the SFRs and evolution of massive starbursting galaxies (e.g., Kaviraj et al. 2015; Sparre & Springel 2016; Pearson et al. 2019; Patton et al. 2020).

Previous studies using optical, near-infrared imaging, or Lyman- $\alpha$  emission in the environment of high-redshift starburst galaxies and quasars have yielded conflicting results. Some of these systems show little or no evidence of companion sources (e.g., Willott et al. 2005; Bañados et al. 2013; Mazzucchelli et al. 2017; Yue et al. 2019), while others find overdensities (e.g., Carilli et al. 2013; Husband et al. 2015; Fan et al. 2016). However, in the last decade, an increasing number of companion sources around high-redshift galaxies have been discovered with the Atacama Large Millimeter/Submillimeter Array (ALMA), primarily using [C II] observations (e.g., Oteo et al. 2016; Trakhtenbrot et al. 2017; Decarli et al. 2017; Díaz-Santos et al. 2018; Wardlow et al. 2018; Casey et al. 2019; Jones et al. 2019; Litke et al. 2019; Neeleman et al. 2019; Fogasy et al. 2020; Venemans et al. 2020). Díaz-Santos et al. (2018) studied the hot dust-obscured galaxy<sup>1</sup> (Hot DOG) W2246–0526 and found evidence of a “gas-bridge” structure between a companion source and the central source, suggesting interaction-induced gas flow in the system. The system BRI 1202–0725 has also been found to host multiple companions to the quasar and exhibits a similar bridge structure (Carilli et al. 2013).

Studies of the effect of AGNs have demonstrated that galactic-scale outflows and feedback can control star formation activity and black hole growth (e.g., Fabian 2012; King & Pounds 2015; Ishibashi & Fabian 2016). The extent of this phenomena is unknown, but recent studies of both low- and high-redshift galaxies show many of these sources exhibit outflow characteristics (e.g., Heckman et al. 1990; Rupke et al. 2005; Weiner et al. 2009; Banerji et al. 2011; Cicone et al. 2014; Chisholm et al. 2015; Spilker et al. 2020) through, for example, blueshifted absorption lines, P Cygni line profiles, or broad emission line components typically seen at higher absolute velocities away from a main emission line. However, these findings become increasingly rare at higher redshifts due to the difficulty in detecting and determining outflow signatures in high-redshift galaxies. Although direct observations of individual sources with outflows are still rare at  $z > 4$  (e.g., Maiolino et al. 2012; Cicone et al. 2015; Spilker et al. 2020; Butler et al. 2021), studies using stacking of the [C II] line have provided an alternative method of searching for outflows in a wider variety and number of sources, though also providing conflicting results (e.g., Gallerani et al. 2018; Decarli et al. 2018; Bischetti et al. 2019; Stanley et al. 2019; Ginolfi et al. 2020).

The strength of the [C II] line facilitates its ubiquitous use at high redshift. At high redshifts, this line is shifted to the millimeter (mm) or submillimeter (sub-mm) regime where it is observable by ground-based facilities such as ALMA. The [C II] ( $^2P_{3/2} \rightarrow ^2P_{1/2}$ ) emission is produced primarily in photodissociation regions (PDRs) by gas exposed to ultraviolet (UV) radiation and acts as one of the major coolants in star-forming regions of the interstellar medium (ISM; e.g., Stacey et al. 1991, 2010; Carilli & Walter 2013). For this reason, it has long been utilized to study the ISM of high-redshift galaxies.

Although magnetic fields are common, their presence and role in galaxy formation and evolution in the early Universe is still unclear. In the local Universe, ordered magnetic fields with a strength of several  $\mu\text{G}$  are revealed from synchrotron and Faraday rotation observations (e.g., Beck 2015) in normal spiral galaxies. In local starburst galaxies, fields as high as  $\sim 20$  mG have been measured (Robishaw et al. 2008), and ordered magnetic fields have been found using infrared (IR) dust polarization observations (e.g., Lopez-Rodriguez et al. 2021). Exactly when these fields were generated is unclear, but models show that a strong regular field can quickly be generated from an initial weak seed field as a result of turbulence driven by, for instance supernova explosions (Rieder & Teyssier 2017). Since atoms and ions can easily be aligned by radiation and are subsequently very sensitive to realignment under the influence of only a weak magnetic field, the strength of the [C II] line has led to the suggestion that [C II] could be an excellent tracer of magnetic fields (Yan & Lazarian 2006; Zhang et al. 2015).

In order to better constrain massive galaxy evolution at high redshift, high-sensitivity data is required to find faint emission from companion sources and to resolve the detailed physics ongoing within these systems. In this study, we explored the environment, searched for magnetic-field signatures, and examined possible outflow properties of two galaxies in the early Universe: the quasar BRI0952–0115 (hereafter BRI0952) at  $z = 4.433$  and the massive submillimeter galaxy (SMG) AzTEC-3 at  $z = 5.3$ , utilizing high-resolution ALMA band-7 [C II] observations. These data were obtained through a proposal designed to look for magnetic fields in the early Universe and were selected based on their previously known extremely bright [C II] emission. Due to the nature of the original project, the sources were observed in full polarization mode in an attempt to detect polarized emission from these sources.

The AzTEC-3 protocluster has been extensively studied previously and encompasses the SMG itself (AzTEC-3) along with a quasar 13 Mpc away in projected distance and a number of previously reported Lyman-break galaxies (LBGs) surrounding the SMG (Capak et al. 2011; Riechers et al. 2014). BRI0952 is a gravitationally lensed quasar and has previously been studied due to its strong [C II] emission and lensing features (Maiolino et al. 2009; Gallerani et al. 2012). Here, we present findings of resolved [C II] emission in both sources, along with an analysis of their surroundings. These findings help shed light on the role both sources have to play in the evolution of massive galaxies in the early Universe.

In Sect. 2, we describe the ALMA observations and analysis utilized in this paper. In Sect. 3, we describe the results from the [C II] line and continuum analysis and the polarization of both AzTEC-3 and BRI0952. Section 4 provides a discussion of the properties of both sources as well as the environment these sources reside in. Finally, we present our conclusions in Sect. 5. Throughout this paper, we adopt the term “outflows” to describe the high-velocity flow of gas away from central regions typically associated with energy-driven winds by central AGNs or through starburst activity. Similarly, the term “gas-bridge” is used to describe structures of gas connecting components within galaxy systems thought to be caused by physical interactions between these components. Furthermore, we utilized a flat  $\Lambda$ CDM cosmology with  $H_0 = 70 \text{ km s}^{-1} \text{ Mpc}^{-1}$ ,  $\Omega_M = 0.3$ , and  $\Omega_\Lambda = 0.7$ .

## 2. Observations and analysis

We obtained ALMA band-7 data for BRI0952 and AzTEC-3 as part of a program originally designed to search for magnetic

<sup>1</sup> Hot dust-obscured galaxies are a class of high-redshift, dust-obscured, AGN-dominated galaxies.

**Table 1.** ALMA band-7 observation details for BRI0952 and AzTEC-3.

Source	Date [yyyy mm dd]	$N_{\text{ant}}$ [GHz]	$\nu_{\text{spw, central}}$ ["×"]	Synthesized beam [mJy beam <sup>-1</sup> ]	Image rms [km s <sup>-1</sup> ]
BRI0952 <sub>[CII]</sub>	2019 04 06	41	349.8	$0.48 \times 0.35$	0.5
BRI0952 <sub>Cont</sub>			336.0, 338.0, 348.0	$0.53 \times 0.41$	0.05
AzTEC-3	2019 03 22	48	301.7	$0.80 \times 0.56$	0.2
AzTEC-3 <sub>Cont</sub>			288.0, 289.9, 299.9	$0.91 \times 0.65$	0.02

**Notes.** We note that these correspond to images created using a robust factor of 0.0.

field lines in the early Universe (2018.1.01536.S, P.I. Vlemmings). The setup for both galaxies was tuned to the [C II] 1900.5369 GHz line, and the “time domain mode” was used. Observation details are listed in Table 1.

The data calibration steps were performed following the ALMA polarization calibration scripts using CASA 5.4.0. (CASA<sup>2</sup>). This includes calibration of the phase, bandpass, flux, and gain. The phase calibrators used for BRI0952 were J0948+002, J0854+2006, and J0725–0054, and for AzTEC-3 these were J0854–2006 and J0948+0022. The quasar J0854+2006 was used for polarization calibration. The uncertainty on the absolute flux calibration is conservatively estimated to be 10%.

To analyze the Stokes-*I* data, imaging was done using the task TCLEAN. All sources in the field were masked during cleaning. An initial search for line emission was done using “dirty” images to identify the line-free channels available for use in continuum subtraction, which was subsequently performed using the UVCONTSUB task with a polynomial fit of the order of one for both AzTEC-3 and BRI0952 (see Figs. A.1 and A.2). The continuum subtraction for BRI0952 was complicated by the appearance of unexpected lines in spectral windows adjacent to that of the [C II] line<sup>3</sup>.

In the case of AzTEC-3, we used the frequency range of the observations up to 300 GHz due to the possible additional [C II] wing feature seen in the 300.5–301 GHz range and the width of the [C II] line (see Figs. 8 and A.1). In the case of BRI0952, we used the frequency ranges 335.3–336.9, 347.1–347.7, 348.97–348.98, and 350.45–350.67 GHz. Line emission images were created from the continuum-subtracted data, and continuum images were made from line-free channels. We used Briggs weighting with a robust factor of 0.5 initially for both AzTEC-3 and BRI0952. However, for further analysis of the companion sources surrounding both primary targets, a robust factor of 0.0 was utilized to increase the angular resolution of the [C II] emission cubes; these images were subsequently used for the analyses described in this paper. The continuum images were created using a robust factor of 0.5. For BRI0952, the spectral window centered on the [C II] emission had a bandwidth of 1.8 GHz with a spectral resolution of 31 MHz. The adjacent spectral windows had bandwidths of 2.0 GHz with spectral resolutions of 15.625 MHz. For AzTEC-3, the spectral window centered on the [C II] emission and the adjacent spectral windows had bandwidths of 2.0 GHz with a spectral resolution of 31.25 MHz. Angular resolution and sensitivity is listed in Table 1.

Polarization image cubes were created at native spectral resolutions of 15.625 MHz and 31.25 MHz channels for BRI0952

**Table 2.** Linear polarization 3 $\sigma$ -limits.

Source	$P_{1, \text{peak}}$ ([C II])	$P_{1, \text{int}}$ ([C II])	$P_{1, \text{dust}}$
BRI0952	<4.8%	<0.7%	<2.7%
AzTEC-3	<2.1%	<0.2%	<2.1%

and AzTEC-3, respectively, using Briggs weighting with a robust factor of 0.5. For BRI0952, the resulting beam size was  $0.51'' \times 0.40''$  with a position angle of  $81^\circ$ . For AzTEC-3, the mean was  $0.91'' \times 0.64''$  (at  $82^\circ$ ). The different observing conditions and channel width resulted in a channel rms noise in the Stokes *Q* and *U* maps of  $0.46 \text{ mJy beam}^{-1}$  and  $0.14 \text{ mJy beam}^{-1}$  for BRI0952 and AzTEC-3, respectively.

For further analysis, including spectral energy distribution (SED) fitting, additional photometry was extracted from archival resources for both AzTEC-3 and BRI0952. *Hubble* Space Telescope (HST) data were extracted from the HST archive for both sources. For AzTEC-3, we used the ACS *F606W*, ACS *F814W*, WFC3 *F105W*, WFC3 *F125W*, and WFC3 *F160W* bands from the following project codes: 13641 (PI: Capak), 9822 (PI: COSMOS24-21), and 13384 (PI: Riechers). For BRI0952, we used the WFPC2 *F814W* band with project code 8268 (PI: Impey), cross-checked the astrometry with the *Gaia*2 catalog (Gaia Collaboration 2018), and used photometry from the WISE All-Sky Data Release (Cutri et al. 2012). We performed an archive search for the MIPS 24  $\mu\text{m}$  data. We used archival data of ALMA bands 3, 4, and 6 (2017.1.01081.S P.I. Leung and 2015.1.00388.S P.I. Lu).

### 3. Results

#### 3.1. Polarization

Our full polarization observations did not reveal any polarized emission, neither from emission lines nor from the source continuum. In Table 2, we indicate the 3 $\sigma$  upper linear polarization ( $P_1$ ) limits that we derive for both sources at the peak for the [C II] line, both for the total integrated line and for the continuum.

The linear polarization spectra and continuum values were extracted in a single beam (see Sect. 3.1 for the size) towards the peak of the lines and continuum, respectively. The linear polarization spectrum was produced from the *Q* and *U* spectra using  $I_p = \sqrt{Q^2 + U^2} - \sigma_p$ , where  $\sigma_p = \sqrt{\sigma_Q^2 + \sigma_U^2}$  corresponds to the rms error on the linear polarization and  $\sigma_{Q,U}$  are the rms errors in *Q* and *U*, respectively. Since we detect no polarization, the derived limits include any potential remaining calibration uncertainty. According to ALMA specifications, this 3 $\sigma$  limit corresponds to 0.1%. Thus, the derived upper limits on the [C II] lines are significantly below values that could be expected if the

<sup>2</sup> <http://casa.nrao.edu/> (CASA McMullin et al. 2007).

<sup>3</sup> We note that the results of this paper do not change when using other tools such as IMCONTSUB or STATCONT (Sánchez-Monge et al. 2018).



**Table 3.** Model lensing parameters for the foreground galaxy of BRI0952.

RA [J2000]	Dec [J2000]	$x_L$ ["]	$y_L$ ["]	$M$ [ $M_\odot$ ]	$e_L$	$\phi_L$ (deg. E of N)	$\gamma$	$\phi_\gamma$ (deg. E of N)	$\mu$
09:55:00.1	-01:30:07.1	0.446	0.003	$0.619 \times 10^{11}$	0.055	191	0.011	63	$3.92 \pm 1.3$

**Notes.** From left to right: ( $x_L$ ,  $y_L$ ) is the position of the source relative to the ALMA phase center given in the first two columns, with positive values corresponding to west;  $M$  is the mass of the lens galaxy;  $e_L$  is the ellipticity;  $\phi_L$  is the position of the major axis in degrees east of north;  $\gamma$  is the external tidal shear;  $\phi_\gamma$  is the position angle of the shear, and  $\mu$  is the derived lensing factor. Since the values were fixed during fitting of the source position, we do not report their respective errors. The magnification factor is taken to be the average across the line.

level of polarization in our sources is similar to that predicted around Galactic star-forming regions (Zhang & Yan 2018).

### 3.2. BRI0952-0115

#### 3.2.1. Lensing magnification

The quasar BRI0952 is lensed by a single galaxy, with the lensing source at  $z = 0.632$ . Although previous lensing models have been constructed for BRI0952 (Lehár et al. 2000; Eigenbrod et al. 2007; Gallerani et al. 2012; Momcheva et al. 2015), the wing-like structures we observe in the [C II] emission suggested differential lensing across the apparent surface of BRI0952 (seen in Fig. B.1), prompting us to create an updated lensing model using our high-resolution data. Additionally, the presence of two companion sources in close proximity to the quasar were also a factor as it was necessary to determine if these represented one double-imaged object or two or more separate sources.

We determined the lensing parameters of both the source and the lens by utilizing VISILENS (Spilker et al. 2016). This code is designed specifically to model observations of gravitationally lensed sources at radio and millimeter wavelengths. VISILENS calculates the magnification factor by directly modeling the  $uv$  data rather than introducing bias by using images produced from algorithms such as CASA’s CLEAN. We modeled the lens as a single isothermal ellipsoid parameterized by its location relative to the ALMA image phase center ( $x_L$ ,  $y_L$ ), the ellipticity ( $e_L$ ), and position angle of the major axis ( $\phi_L$ ) in degrees east of north. We modeled the source as a Sérsic source parameterized by position relative to the lens ( $x_S$ ,  $y_S$ ), flux density, Sérsic index, half-light radius, axis-ratio, and position angle. These parameters are then run through a Markov chain Monte Carlo (MCMC) fitting procedure, and the best models were output using a deviance information criterion as described in Spilker et al. (2016).

Initially, we ran VISILENS on band-7 continuum data in order to determine the best-fit parameters for the lens. Although lens parameters have been previously reported (Lehár et al. 2000; Eigenbrod et al. 2007; Gallerani et al. 2012; Momcheva et al. 2015), lens fitting was improved when we allowed the parameters to vary outside of previous values. During the lens optimization, we also allowed the source to vary in position and flux density. Once the lens was optimized, we reran the continuum fit with fixed lens parameters but still allowed the Sérsic source profile to vary. Similarly, for the band-7 [C II] emission data, we ran VISILENS with the previously optimized lens parameters on the  $uv$  line emission data while allowing the source to vary in an attempt to increase the quality of our lensing model. The model produced by VISILENS is a good fit for our data with minimal to no residual emission, and this is shown in Fig. B.1. The best-fit parameters are provided in Table 3. Furthermore, the magnification factor produced from this model is similar to those previously reported ( $\mu \sim 3.92 \pm 1.3$ ).

The presence of wing-like structures across the [C II] frequency range of our BRI0952 observations, as seen in the [C II] line emission map (see Fig. B.1, panels 1 and 3 for observed [C II] data and model output of VISILENS), prompted consideration of the effect of different lensing factors across the line (i.e., differential magnification). To investigate this, we split the [C II] line into five bins constituting five different frequency ranges across the line (these can be seen in Fig. B.1) and ran VISILENS, with the source and lens parameters as specified above, on these bins. The results of this are shown in Fig. B.1. We determine that it is likely that some amount of differential lensing across the surface of BRI0952 is occurring, and thus we caution that conclusions drawn that correlate strength of emission with location will be affected by this. However, we conclude that based on the low lensing-magnification factor, this effect will not drastically change the extent or strength of the [C II] or continuum emission studied in this paper.

We also note that images of both the data and residuals, as seen in Figs. B.1 and C.1 are produced by VISILENS rather than by CASA. Although the imaging process in itself is similar to the procedure that CASA performs, it lacks the ability to change weighting schemes and does not clean images. Thus, images produced in VISILENS are dirty images with natural weighting and therefore will look slightly different than those created by CASA. As a consequence of this, faint sources in close proximity to BRI0952 are not clearly resolved and distinguishable in images produced by VISILENS. This is in contrast with images produced in CASA, which are cleaned with a Briggs weighting scheme using a robust factor of 0.0. The latter are those used throughout the spectral analysis in this paper.

#### 3.2.2. [C II] emission

We detect [C II] ( $^2P_{3/2} \rightarrow ^2P_{1/2}$ ) line emission toward both images of the lensed quasar BRI0952. We refer to the two images of the quasar as the “north” and “south” images (names and locations shown in Fig. 1). We confirm the detection of a southern companion source (henceforth termed Comp-SW) tentatively detected by Gallerani et al. (2012); we note that our detection is located in the same region as that of the source reported by Gallerani et al. (2012), but at a significantly lower signal-to-noise ratio (S/N) and a smaller emitting region. Furthermore, we tentatively detect a second companion (termed Comp-N) north of the top image of the quasar. Higher resolution data and a source plane reconstruction of this system would be required to come to a robust conclusion about the nature of this emission. For the purposes of this paper, we treated both sources as additional companion galaxies as the emission is not seen in our lensing model produced by VISILENS, which suggests it is not simply an affect of the lensing magnification. We isolated our lensing model to only those velocities in which the companions manifest and demonstrate in Fig. C.1 that “residual” emission

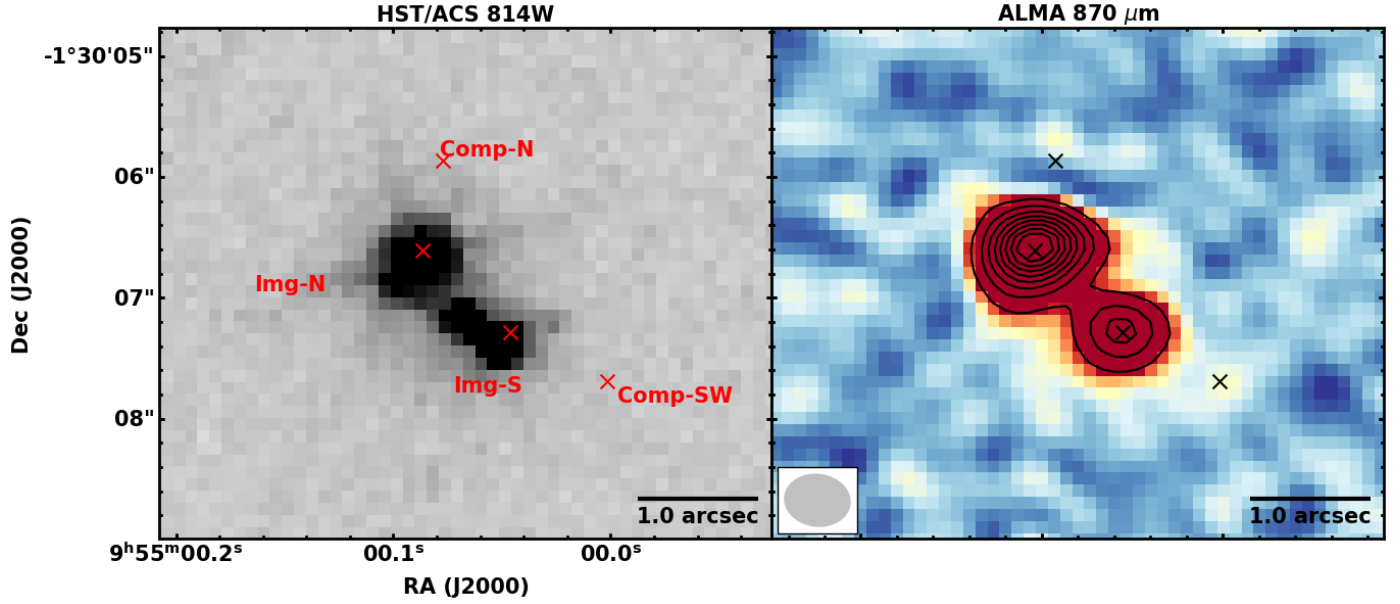


**Fig. 1.** HST/ACS  $F814W$  (left) image of BRI0952 showing both lensed images of the quasar; Img-N and Img-S correspond to the two images of the quasar BRI0952 and Comp-N and Comp-SW to the companion sources. ALMA  $870\,\mu\text{m}$  continuum map (right) was created using line-free channels. The contours are shown at 5, 10, 20, 30, 40, 50, 60, 70, and  $80\sigma$  levels. The synthesized beam is shown in the bottom left of the ALMA image.

remains in the regions of the companions, lending further weight to the conclusion that the emission has a separate origin to that of the quasar. Given the relatively lower S/N of Comp-N and Comp-SW in relation to BRI0952, combined with the fact that the lensing model reproduces the flux of BRI0952 using a single Sérsic brightness distribution, we treated Comp-SW and Comp-N as not sufficiently lensed to affect conclusions drawn in this analysis (in effect  $\mu_{\text{Comp-N}} = \mu_{\text{Comp-SW}} = 1$ ).

We note that including additional faint sources in the lensing analysis with VISILENS did not enable a good fit for the two companion sources; however, given their location, they are likely to be magnified by a factor close to  $\mu \sim 1$ . Furthermore, based on the close spatial proximity of Comp-SW and Comp-N to BRI0952, we assume the emission is [C II] and find spectroscopic redshifts of  $z_{\text{Comp-SW}} = 4.4323$  and  $z_{\text{Comp-N}} = 4.432$ .

To extract the spectra of BRI0952, Comp-N, and Comp-SW we defined a region around each from which to extract the [C II] spectra individually for each component<sup>4</sup>. For BRI0952, we used an elliptical region of  $2.1'' \times 1.45''$  encompassing  $\sim 18$  beams<sup>5</sup>, containing both Img-S and Img-N of the quasar. For Comp-SW, we used an elliptical region of  $1.13'' \times 0.57''$  encompassing  $\sim 4$  beams, and for Comp-N we used an elliptical region of  $1.3'' \times 0.62''$  encompassing  $\sim 5$  beams. These regions are shown in Fig. 2 along with moment-0 and moment-1 maps, and extracted spectra are shown in Fig. 3. Both companions are faint compared to the emission from BRI0952; both are  $\leq 10\%$  of the flux from BRI0952 (see Fig. 6). The gray plotted rms in Fig. 3 is calculated in each channel by sampling the spectra in 25 different emission-free regions of the cube extracted from regions

the same size as those described above for each individual source.

Due to the presence of high-velocity wings at an  $\sim 14\sigma$  level in the spectra of BRI0952, we find that a double-Gaussian fit was more appropriate (see Fig. 3, top panel), yielding an improvement to the reduced  $\chi^2$  of more than a factor of four. To investigate the impact of differential magnification on the broad wings and attempt to determine if this feature is simply an artifact from lensing, we calculated the ratio of the flux in the blue and red wings of the line profile. If the ratio of the blue to red wing is more than the error on the lensing factor, we suggest that the broad wings could be due to differential magnification predominantly affecting one side of the line. We define these wings to be between  $\pm 500\,\text{km s}^{-1}$  and  $1/4 \times F_{\text{peak}}$ , where  $F_{\text{peak}}$  is the peak of the flux. We find the ratio of the red-to-blue wing to be  $\sim 1.09$ , which is less than the error on the magnification factor (1.3). This suggests that while the observed broad velocity wings may be slightly affected by lensing magnification, it is not solely responsible for them. As an additional test, we extracted the spectra from a region only corresponding to Img-N of BRI0952 to determine if the double Gaussian remained a better fit to the data (shown in Fig. D.1). Indeed, the broad wings remain, and a double Gaussian provides an improved fit to the data. We further discuss the implications of this in Sect. 4.5.

We compare the line intensities of each component to those found by Gallerani et al. (2012). We find that our values are lower, both for the intensity of BRI0952 and for Comp-SW (their Comp-C). However, we note a significant discrepancy between their decomposition and ours. Gallerani et al. (2012) find that Comp-SW is significantly brighter than either of the individual images of the quasar BRI0952 (here Img-N and Img-S), while we find the opposite to be true. We attribute this to the increased spectral resolution and baseline coverage possible with ALMA over the IRAM Plateau de Bure Interferometer (PdBI).

The observations from Gallerani et al. (2012) were carried out with the IRAM Plateau de Bure Interferometer with six

<sup>4</sup> This extraction could be done through a number of different methods; however, we find that the outcomes of these methods remain consistent with the method employed in this paper. We also note that methods such as  $uv$ -plane fitting introduce bias in a similar way to image-plane fitting through base-assumptions of, e.g., a model to describe the source, boundary conditions, and so on.

<sup>5</sup> We define  $N_{\text{beams}} = A_{\text{extraction}}/A_{\text{beam}}$ .

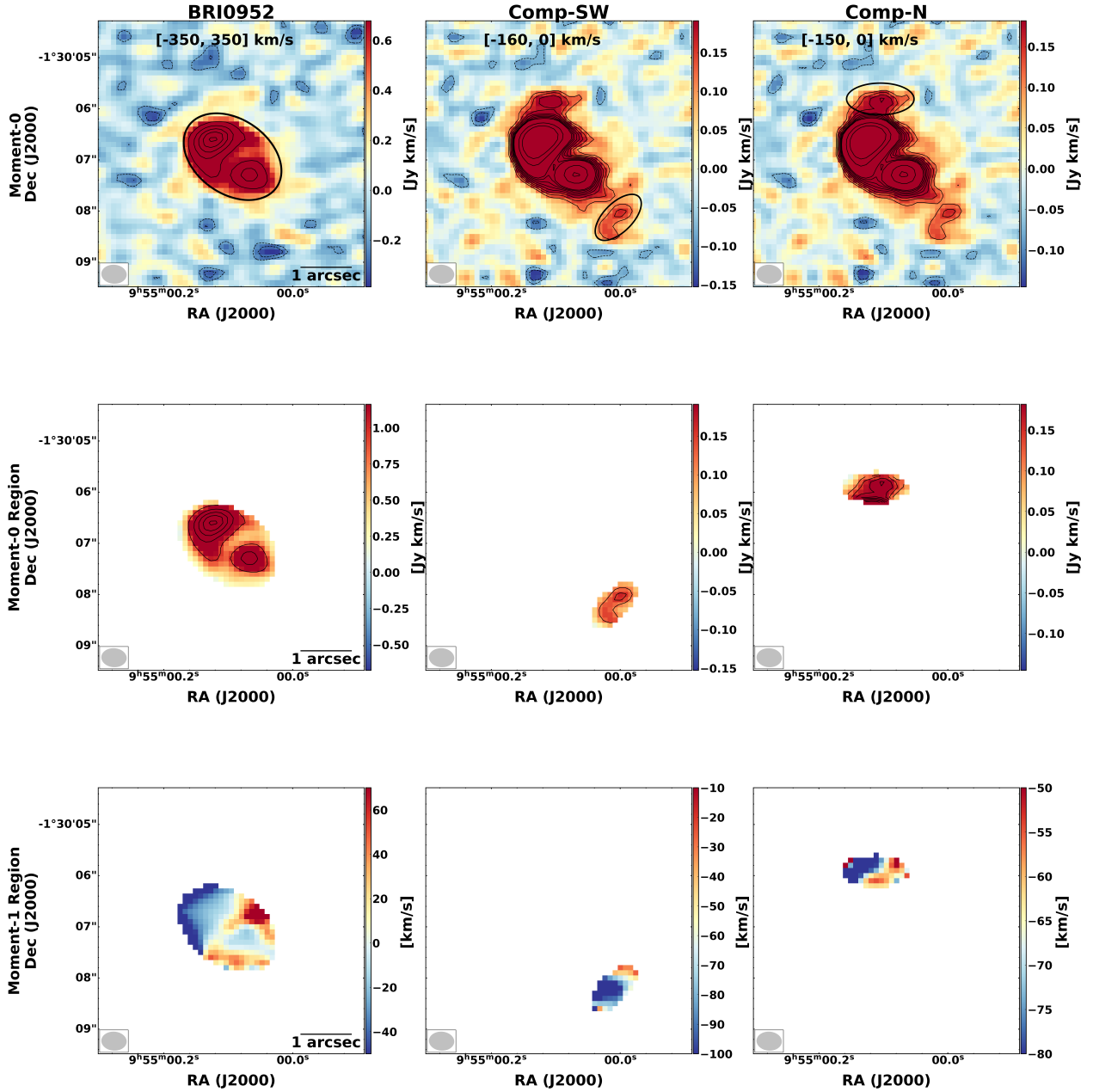


**Fig. 2.** Moment-0 and moment-1 maps for the BRI0952 system. The top row shows moment-0 maps of the original [C II] with velocity ranges for the individual extraction shown on the image. The middle row shows the moment-0 map of the region from which the spectra was extracted for the companions. The bottom row shows the moment-1 maps for the sources taken from the same region the spectra was extracted from. The contours are shown at  $-3$ ,  $-2$ ,  $10$ ,  $20$ ,  $30$ ,  $40$ ,  $50$ , and  $60\sigma$  levels for BRI0952, and contours are at  $-3$ ,  $-2$ ,  $3$ ,  $4$ ,  $5$ ,  $6$ , and  $7\sigma$  levels for the companions where the respective  $1\sigma$  noise level has been taken from individual moment-0 maps due to the restrictive velocity ranges (and thus differing noise levels). The black ellipses in the top row correspond to the region from which the spectra was extracted. The synthesized beam is shown in the bottom left corner of the images.

antennas in the extended B configuration during three observing runs and the compact C configuration during two observing runs. They obtained a sensitivity level of  $0.5 \text{ Jy km s}^{-1} \text{ beam}^{-1}$  in a  $300 \text{ km s}^{-1}$  channel, which corresponds to a  $1\sigma$  rms of  $1.7 \text{ mJy beam}^{-1}$ . For comparison, our ALMA data for a similar channel width would be  $\sim 0.1 \text{ mJy beam}^{-1}$ , which is about 15–17 times better in terms of sensitivity. We note that the BRI0952 field is near equatorial, meaning that many antennas possibly in combination with several antenna configurations are needed to achieve a good  $uv$ -coverage in the  $v$  direction. Given the higher sensitivity combined with the improved  $uv$  cover-

age thanks to the larger number of ALMA antennas, it is likely that the calibration and image reconstruction of the ALMA data is more robust. As a further comparison between the previous PdBI observations from [Gallerani et al. \(2012\)](#) and the new ALMA observations, the spatial resolution is  $1.08'' \times 0.66''$  and  $0.54'' \times 0.40''$ , respectively, and the absolute flux calibration is  $\sim 20\%$  and  $\sim 10\%$ , respectively.

We used CASA's IMFIT task to fit the source size for both images of the quasar and companions. We provide [C II] line parameters and deconvolved source sizes in Table 4. We note that, due to the lensed nature of BRI0952, this source has a

**Table 4.** Line parameters for the [C II] emission lines.

Name	RA [J2000]	Dec [J2000]	Distance ["]	$z_{\text{[CII]}}$	$I_{\text{[CII]}}$ [Jy km s <sup>-1</sup> ]	$FWHM_{\text{[CII]}}$ [km s <sup>-1</sup> ]	$A_{\text{[CII]}}$ ["''"]
BRI0952	N: 09:55:00.10 S: 09:55:00.06	-01:30:06.61 -01:30:07.29	1.0	4.433	$15.45 \pm 1.5$	$182 \pm 5$ $410 \pm 21$	$([0.51 \pm 0.19] \times [(0.285 \pm 0.12)])$ $([0.36 \pm 0.13] \times [0.29 \pm 0.21])$
Comp-N	09:55:00.09	-01:30:05.89	0.75	4.432	$0.62 \pm 0.06$	$130 \pm 10$	$([0.79 \pm 0.32] \times [0.23 \pm 0.11])$
Comp-SW	09:55:00.00	-01:30:08.05	2.2	4.432	$0.30 \pm 0.04$	$122 \pm 13$	$([0.76 \pm 0.30] \times [0.23 \pm 0.13])$
AzTEC-3	10:00:20.696	+02:35:20.35		5.2988	$11.34 \pm 1.0$	$320 \pm 12$ $660 \pm 20$	$([0.69 \pm 0.06] \times [0.42 \pm 0.10])$
LBG-3	10:00:20.766	+02:35:21.39	1.5	5.2841	$0.78 \pm 0.07$	$630 \pm 36$ $165 \pm 24$	$([0.8 \pm 0.02] \times [0.46 \pm 0.02])$
Gal-S	10:00:20.68	+02:35:18.07	2.3	5.2919	$0.52 \pm 0.05$	$190 \pm 10$ $92 \pm 23$	$([0.53 \pm 0.10] \times [0.41 \pm 0.15])$
Gal-SW	10:00:20.60	+02:35:19.28	1.8	5.2942	$0.15 \pm 0.01$	$325 \pm 24$	$([0.36 \pm 0.04] \times [0.08 \pm 0.10])$

**Notes.** The distance is measured between the central source (AzTEC-3 and the northern image of BRI0952, respectively) and the surrounding sources.  $I_{\text{[CII]}}$  is the line intensity, and FWHM is the full width at half maximum of the lines (one entry for single-Gaussian fit and two entries for double-Gaussian fit).  $A_{\text{[CII]}}$  is the length of the major axis of the deconvolved source size from CASA's IMFIT, we note that BRI0952 has a more complex morphology, and thus the sizes include an additional 30% error on the reported value corresponding to the uncertainty on the lensing factor.

more complex morphology than those typically handled in this way. The source size provided from IMFIT is an indication of the extent of the emission in the image plane and is not necessarily well fit by a Gaussian profile. We added an additional 30% on the error of the spatial extent of the emission reported for Img-S and Img-N corresponding to the uncertainty on the lensing magnification factor.

We note the presence of a complex velocity structure between the images of the lensed quasar and the companions. The northern companion exhibits a faint velocity gradient, and the same is present for the south-western companion (see Fig. 4). The implications of this are further discussed in Sect. 4.6.

### 3.2.3. Continuum

We detect strong continuum emission toward both north and south images of BRI0952. Using CASA's IMFIT, we fit both the north and south images of the quasar and report strong continuum emission totaling  $1.96 \pm 0.43$  mJy, which is corrected for lensing. Continuum fluxes from individual images of the quasar are provided in Table 5 and images are shown in Fig. 1. We do not detect the companion sources in continuum and report a  $3\sigma$  upper limit of 0.13 mJy for each. Due to the non-detection of the companions in the continuum, we defined a region corresponding to the quasar from which to extract the continuum flux. As for the line emission, the source sizes of BRI0952 reported in Table 5 are reported with an additional 30% error added to account for the complex morphology and lensing uncertainties.

Since we do not detect the companions in continuum emission, we estimated their flux using relations from their  $L_{\text{[CII]}}$  to determine if they should be detectable in our ALMA observations. We estimated their SFR's using the relation  $\log(\text{SFR}) [M_{\odot} \text{ yr}^{-1}] = 1.0 - 7.06 \times \log(L_{\text{[CII]}} [L_{\odot}])$  from De Looze et al. (2014) for starburst galaxies, computed their  $L_{\text{IR}}$  using the relation in Sect. 4.3 (Carilli & Walter 2013), and used a modified blackbody approximation (e.g., Knudsen et al. 2003, Eq. (2)) to recover their  $S_{350 \text{ GHz}}$ . This results in  $S_{350 \text{ GHz}} = 0.21$  mJy for the northern companion and  $S_{350 \text{ GHz}} = 0.10$  mJy for the south-western companion. This would correspond to an

$\sim 4\sigma$  detection for the northern companion and an  $\sim 2\sigma$  detection for the southern companion. Thus, in the case of the southern companion with the current data a continuum emission detection is unfeasible. This may also be the case for the northern companion. However, it is also possible that without the velocity information encoded in emission line spectra (and thus without the ability to severely isolate the frequency or velocity range from which to attempt to extract information about the emission from the companions), our observations are simply insufficient to resolve any continuum emission from the companions.

### 3.2.4. SED fitting

We performed IR SED fitting and decomposition of the AGN and star formation contributions, using DecomIR (Mullaney et al. 2011) following the methods of (Stanley et al. 2018). We used photometry from an archival search for WISE bands and MIPS 24  $\mu\text{m}$ . We also used ALMA archival data from bands 3, 4, and 6. We performed two sets of fits, one with only the star formation templates and one with both AGN and star formation templates. We find that the photometry of BRI0952 is best fit by a combination of AGN and star formation emission in the IR. The decomposition of the IR SED allows for a calculation of the SFR without contamination from the AGN emission, using the  $L_{\text{IRSF}}$  integrated from 8–1000  $\mu\text{m}$ . IR luminosities are reported in Table 6 and discussed further in Sect. 4.2.

## 3.3. Aztec-3

### 3.3.1. [C II] emission

We detect [C II] ( $^2P_{3/2} \rightarrow ^2P_{1/2}$ ) emission toward the SMG AzTEC-3. We report three sources (LBG-3, Gal-S, and Gal-SW) of the same emission in the region shown in Fig. 5. LBG-3 was initially detected as an Lyman-break galaxy with the COSMOS survey (Ilbert et al. 2009, optical ID 1447526) but was undetected in [C II] in Riechers et al. (2014) and the authors presented a  $3\sigma$  upper limit on its [C II] emission. An additional companion, LBG-2 – not shown in Fig. 5, was



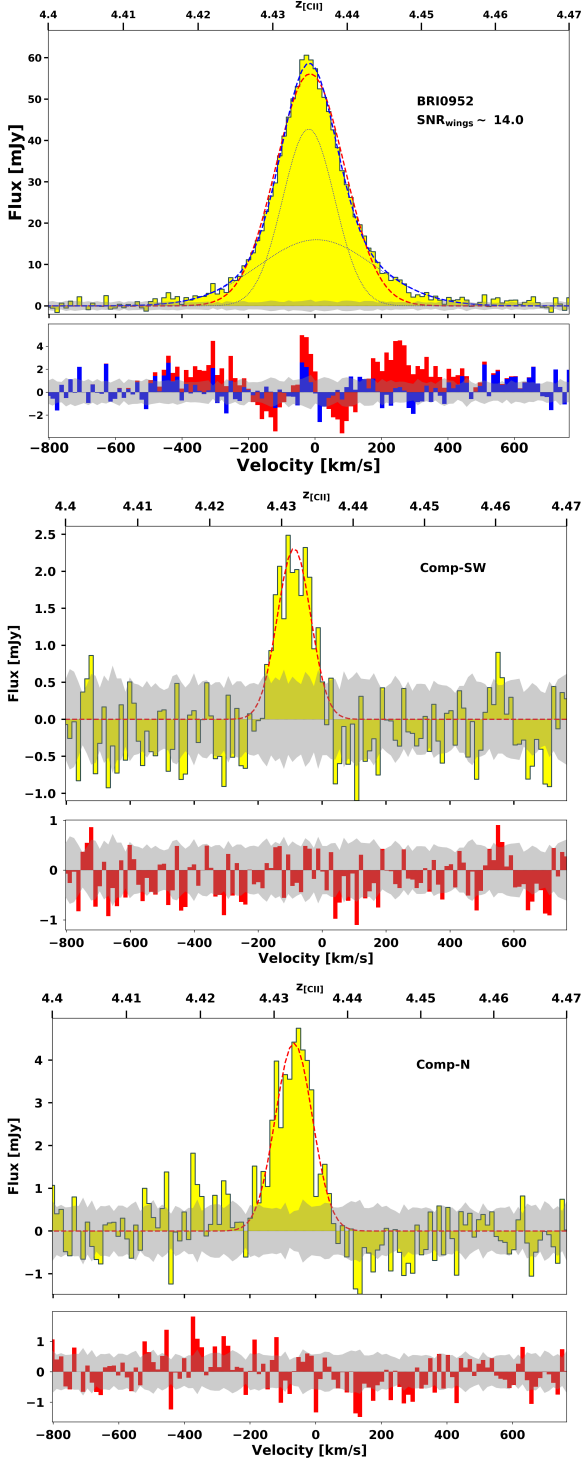


**Fig. 3.** Spectra of [CII] emission toward BRI0952 and companions. The two companions' line profiles are fit with a single Gaussian, which is shown in red. The quasar's line emission profile is fit with a single Gaussian (red) and a double Gaussian (blue); the double Gaussian corresponding to outflow signatures is clearly seen. The gray region represents the rms of the data in each channel using the procedure described in Sect. 3.2.2.

also originally detected by COSMOS as an LBG but was also undetected in [CII] by Riechers et al. (2014). Similarly, we do not detect the source in [CII] emission, and thus do not investigate this source further. Gal-S and Gal-SW are first detections.

**Table 5.** Continuum fluxes for both systems.

Galaxy	Region ["×"]	$S_\nu$ [mJy]
BRI0952 <sub>N</sub>	$([0.35 \pm 0.15] \times [0.20 \pm 0.13])$	$1.44 \pm 0.4$
BRI0952 <sub>S</sub>	$([0.31 \pm 0.15] \times [0.26 \pm 0.13])$	$0.52 \pm 0.14$
Comp-N	–	<0.13
Comp-SW	–	<0.13
AzTEC-3	$([0.38 \pm 0.03] \times [0.27 \pm 0.07])$	$6.06 \pm 0.13$
LBG-3	$([0.59 \pm 0.07] \times [0.35 \pm 0.07])$	$0.19 \pm 0.02$
Gal-SW	$(<0.91 \times <0.66)$	$0.07 \pm 0.02$
Gal-S	–	<0.056
ES	$([1.09 \pm 0.38] \times [0.37 \pm 0.36])$	$0.21 \pm 0.05$

**Notes.** The continuum fluxes are provided for both images of BRI0952 and are corrected for lensing. However, we do not correct the sizes for lensing. We note that the error on the companions of AzTEC-3 includes an additional 10% due to the additional uncertainty introduced from the deblending process and the errors on the size of both images of BRI0952 include an additional 30% to account for lensing uncertainty.

The data of Riechers et al. (2014) were obtained during Cycle-0 with 16–24 antennas, with a total observing near 7000 s spread evenly over two pointings. As a result, the sensitivity of the data in the region around AzTEC-3 is lower by about a factor of two compared to the new data presented here; however, it is important to note that the beam area of our data is  $1.7\times$  larger. We note that the  $3\sigma$  limit from Riechers et al. (2014) appears to be for a single beam, while we obtain a detection over a more extended region corresponding to  $2.8\times$  the size of beam used in this analysis. Furthermore, we note that if converting their  $3\sigma$  upper limit to a  $5\sigma$  upper limit, the resulting  $I_{\text{[CII]}}$  is consistent with our detection, though it is important to keep in mind that in this comparison we do not take into account the integration over an extended area.

We assume that the emission from the companions is [CII] based on their close proximity to AzTEC-3, and find a spectroscopic redshift of  $z_{\text{LBG-3}} = 5.284$ , which is in relative agreement with the previous spectroscopic redshift of  $z = 5.3$  (Riechers et al. 2014). We report spectroscopic redshifts for the additional companions,  $z_{\text{Gal-S}} = 5.2919$  and  $z_{\text{Gal-SW}} = 5.2942$ , respectively. Figure 6 shows the combined spectra of the companions and AzTEC-3.

We followed the same procedure as described for BRI0952 and individually extracted the spectra for the sources in this system from a region with a very limited velocity range<sup>6</sup>. We used a circular region with a radius of  $2.4''$  to extract the spectra of AzTEC-3 encompassing  $\sim 13$  beams. We used elliptical regions for the following companions:  $1.2'' \times 1.5''$  for LBG-3 encompassing  $\sim 4$  beams,  $2.6'' \times 1.7''$  for Gal-S encompassing  $\sim 10$  beams, and  $1.3'' \times 0.90''$  for Gal-SW encompassing  $\sim 3$  beams. These regions are shown in Fig. 7. We were able to minimize the source blending of the companions with AzTEC-3 since the spectra of the companions are extracted over a very limited velocity range, as shown in Fig. 7. We calculated the rms in the same way as described in Sect. 3.2.2. Additionally, we include the atmospheric transmission in the top subplot for every source in Fig. 8 to show where the atmospheric absorption line is (shown in Fig. A.1), specifically in relation to the companion spectra.

<sup>6</sup> Again, similar to BRI0952; if other methods are used, the results remain consistent with the regional spectral extraction used here.

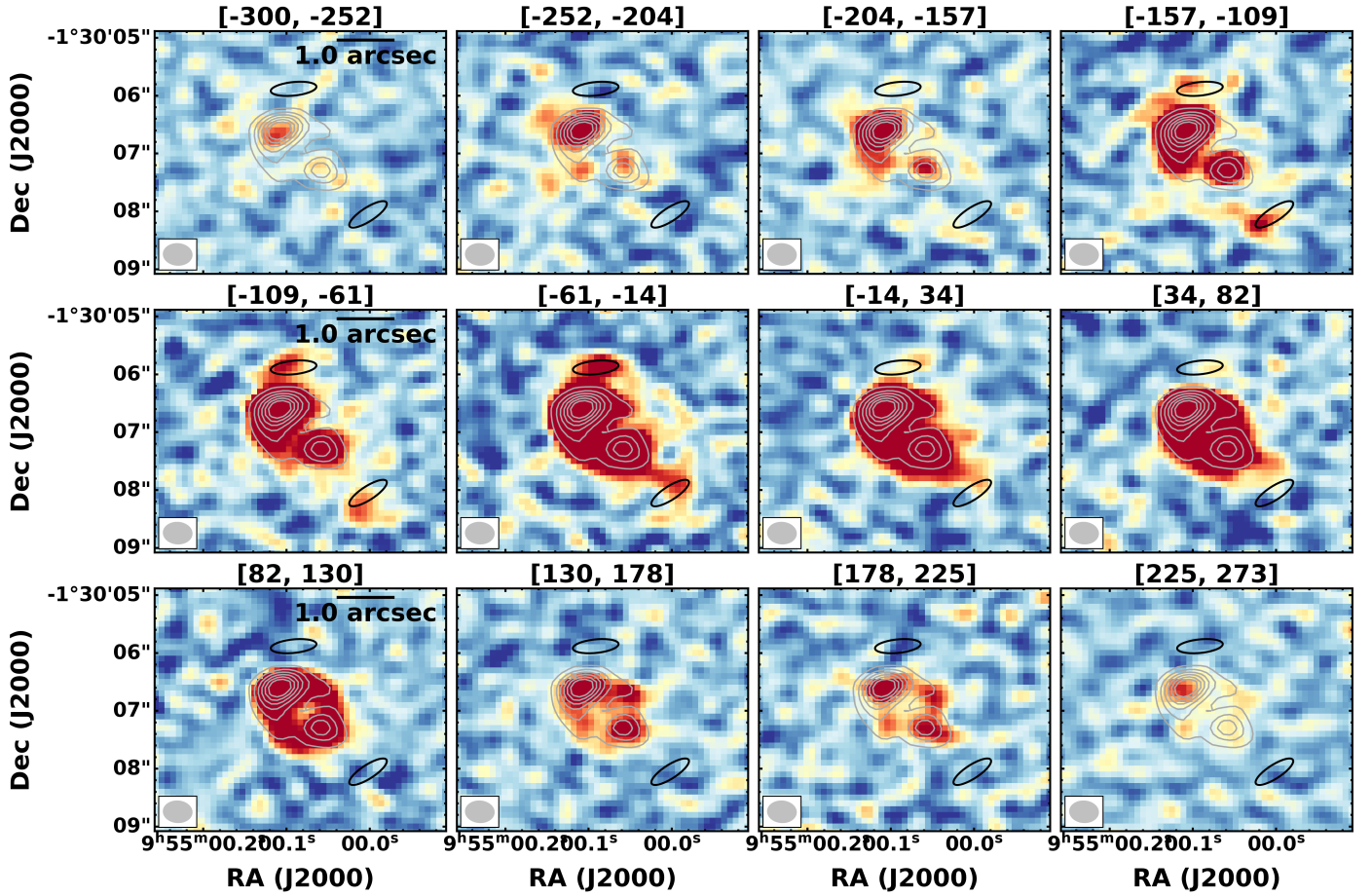


**Fig. 4.** Velocity maps of BRI0952 showing [C II] emission across the velocity range of the line. The velocity range is provided at the top of the images. The gray contours are at 10, 20, 30, 40, 50, and 60 $\sigma$  levels from the moment-0 map of BRI0952, which is shown in Fig. 2. The black ellipses indicate the positions and sizes of the two companions from CASA's IMFIT routine. The southern companion shows a clear velocity gradient across the  $-157$  to  $-14$  km s $^{-1}$  range. The size of the synthesized beam is shown in the bottom left corner of the images.

**Table 6.** Derived properties for sources.

Name	$L_{\text{[CII]}}$ [ $10^9 L_{\odot}$ ]	$L_{\text{IR}}$ [ $10^{12} L_{\odot}$ ]	$\text{SFR}_{\text{IR}}$ [ $M_{\odot} \text{ yr}^{-1}$ ]	$\text{SFR}_{\text{[CII]}}$ [ $M_{\odot} \text{ yr}^{-1}$ ]	$L_{\text{[CII]}}/L_{\text{IR}}$ $10^{-3}$	$\dot{M}_{\text{out}}$ [ $M_{\odot} \text{ yr}^{-1}$ ]	$M_{\text{dyn,[CII]}}$ [ $10^{10} M_{\odot}$ ]
BRI0952	$2.46 \pm 0.23$	$7.66 \pm 2.49$	770	247	0.37	$98 \pm 19$	0.90
Comp-N	$0.39 \pm 0.04$	$<0.2$	$<21$	34	$<2.0$	–	0.5
Comp-SW	$0.19 \pm 0.03$	$<0.2$	$<21$	16	$<1.0$	–	0.4
AzTEC-3	$9.3 \pm 0.80$	$73.4 \pm 2$	7340	809	$0.12 \pm 0.01$	$238 \pm 30$	6.5
LBG-3	$0.63 \pm 0.05$	$0.40 \pm 0.5$	$40 \pm 46$	55	$1.6 \pm 0.14$	–	0.95
Gal-S	$0.43 \pm 0.04$	$<0.1$	$<12.0$	37	$<3$	–	0.83
Gal-SW	$0.12 \pm 0.01$	$0.15 \pm 0.2$	$15 \pm 23$	11	$0.85 \pm 0.13$	–	1.6

**Notes.**  $L_{\text{IR}}$  refers to the integrated IR luminosity from 8–1000  $\mu\text{m}$  for BRI0952 (using  $L_{\text{IR,SE}}$ ) and AzTEC-3 and to a modified blackbody approximation for the companion sources.  $\text{SFR}_{\text{IR}}$  is the SFR derived from the  $L_{\text{IR}}$ ,  $\text{SFR}_{\text{[CII]}}$  refers to the SFR derived from the relation given in De Looze et al. (2014) for starburst galaxies.  $\dot{M}_{\text{out}}$  gives the mass outflow rate, and  $M_{\text{dyn}}$  is the dynamical mass. Upper limits are provided for inferred properties for Gal-S, Comp-N, and Comp-SW as we do not detect these sources in continuum emission. The luminosities reported for BRI0952 are corrected for magnification.

The [C II] spectral line profile of AzTEC-3 shows the presence of high-velocity wings at a  $\sim 24\sigma$  level – and the profile is better fit with a double Gaussian to account for this (Fig. 8) – where the reduced  $\chi^2$  is improved by more than a factor of four using a double-Gaussian fit. We note that the blue wing is wider compared to that of the red wing, as reported in Riechers et al. (2014). We used CASA's IMFIT to determine deconvolved source sizes. We report source sizes and Gaussian line parameters for

AzTEC-3 and companions in Table 4. The [C II] emission from the central source is emitted over a compact region with an extent of  $4.2 \pm 0.4$  kpc along the major axis, which is consistent with the emitting region of 3.9 kpc reported by Riechers et al. (2014). We do not detect a strong velocity gradient, which is also in good agreement with Riechers et al. (2014).

We note an additional feature: a possible velocity gradient between AzTEC-3 and LBG-3. We show this in Fig. 9 and

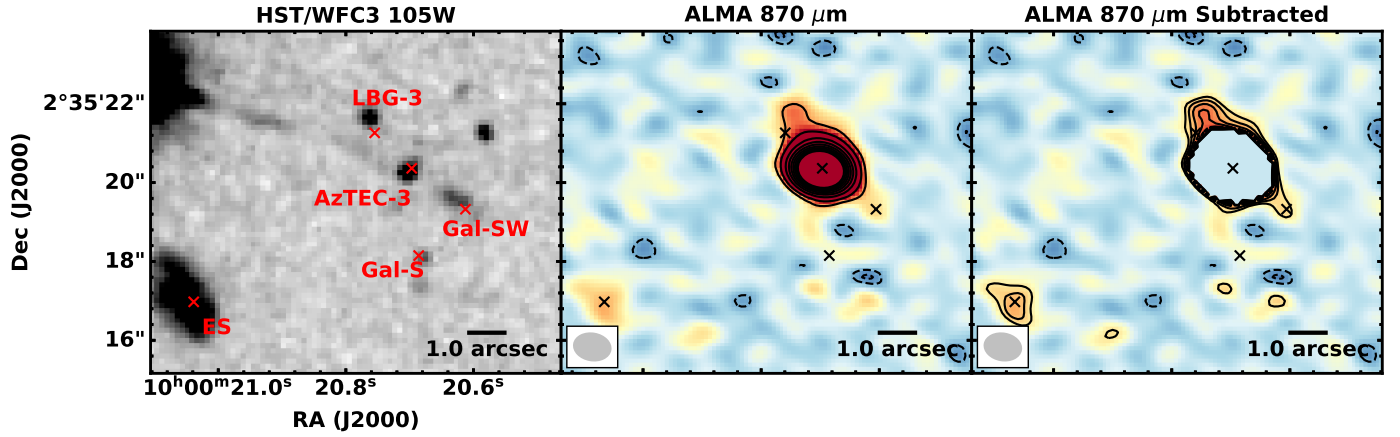


**Fig. 5.** HST/WFC3  $F105W$  (left) image of AzTEC-3 overlaid with source positions, ALMA 850  $\mu\text{m}$  continuum map (center), and SMG subtracted map (right). The continuum maps were created using line-free channels. The residual map was produced following the steps described in Sect. 3.3.2. The original continuum image contours are shown at  $-3, -2, 5, 10, 20, 30, 40, 50, 60, 70$ , and  $80\sigma$  levels. The subtracted image contours are shown at  $-3, -2, 3, 4, 5, 6$ , and  $7\sigma$  levels. Synthesized beams are shown in the bottom left of the ALMA images.

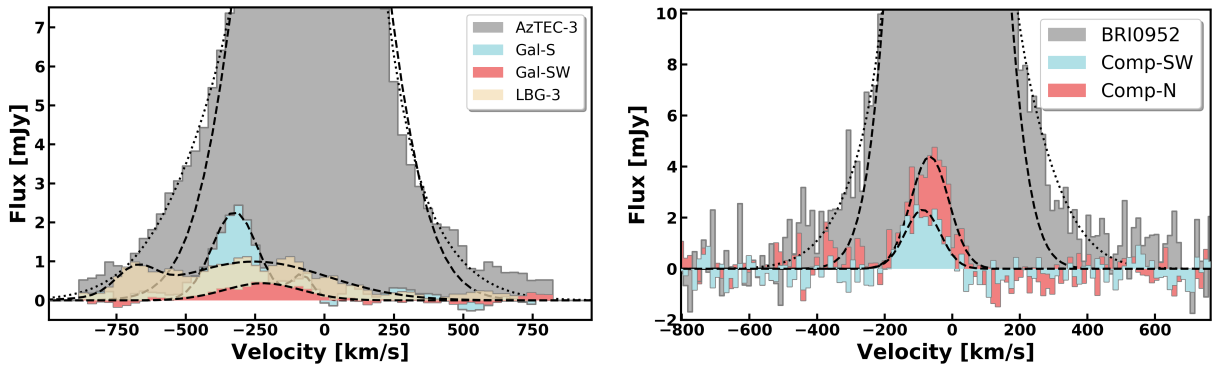


**Fig. 6.**  $[\text{C II}]$  spectra for the companions of BRI0952 and AzTEC-3. The spectra of both the quasar and the SMG have been truncated so that the companion spectra are easily seen. The single- (dashed) and double- (dotted) Gaussian fits for both AzTEC-3 and BRI0952 are overplotted, along with the Gaussian fits to the companion sources. We highlight that the companions to BRI0952 are located at a very similar systemic velocity, whereas AzTEC-3's companions are located in the blue part of the spectrum.

Fig. E.1. This is a tentative feature as it only appears in a few spectral elements and could simply be emission associated with AzTEC-3. Guaita et al. (2022) detected a bridge of Lyman- $\alpha$  emission extending between these two components, indicating that tidal forces could be at work between LBG-3 and AzTEC-3. The detection of Lyman- $\alpha$  in both AzTEC-3 and LBG-3 further supports the likelihood of an interacting system. This is further discussed in Sect. 4.6.

### 3.3.2. Continuum

We obtain continuum emission from imaging line-free channels in the band-7 ALMA data. Due to the lower angular resolution combined with the lack of velocity information provided in the spectral emission, we were unable to isolate the emission from the companions by restricting the velocity range from which they were extracted as we did for the  $[\text{C II}]$  emission. Hence, we extracted the continuum flux using three different methods.

The first was to use CASA's IMFIT routine on the marginally resolved continuum image. From this we obtain a continuum flux of  $6.06 \pm 0.13$  mJy for AzTEC-3, which is in good agreement with Riechers et al. (2014),  $0.071 \pm 0.018$  mJy for Gal-SW, and  $0.18 \pm 0.023$  mJy for LBG-3.

Secondly, we used the IMFIT residual image with the continuum emission from AzTEC-3 removed to obtain the continuum

flux of the companions. Using this method, we obtain a continuum flux of  $0.082 \pm 0.02$  mJy for Gal-SW and  $0.19 \pm 0.024$  mJy for LBG-3.

Finally, we attempted to isolate the origin of the continuum flux for the companions by creating a continuum image corresponding only to the flux from AzTEC-3, which we were then able to subtract from the original continuum image. To model the flux from AzTEC-3, we selected emission that was at levels higher than  $9\sigma$ . This emission was then subtracted from the continuum image. The original continuum image and the subtracted image are shown in Fig. 5. This resulted in a continuum flux of  $0.06 \pm 0.017$  mJy for Gal-SW and  $0.22 \pm 0.025$  mJy for LBG-3. Due to the similarity of the results from various methods, we conclude that the intrinsic value of the continuum for each is in the range provided for the continuum for LBG-3 and Gal-SW.

We do not detect Gal-S in continuum, and we report a  $3\sigma$  upper limit of 0.05 mJy. The companion sources are faint compared to AzTEC-3 ( $\sim 3\%$  for LBG-3 and  $\sim 1\%$  for Gal-SW), and their flux contribution to the central source is negligible. Flux measurements and deconvolved source sizes for the field are provided in Table 5, where average values are provided for LBG-3 and Gal-SW for both continuum flux and size estimates.

We note an offset between the ALMA continuum, HST, and  $[\text{C II}]$  emission for LBG-3. This is shown in Fig. F.1. We suggest

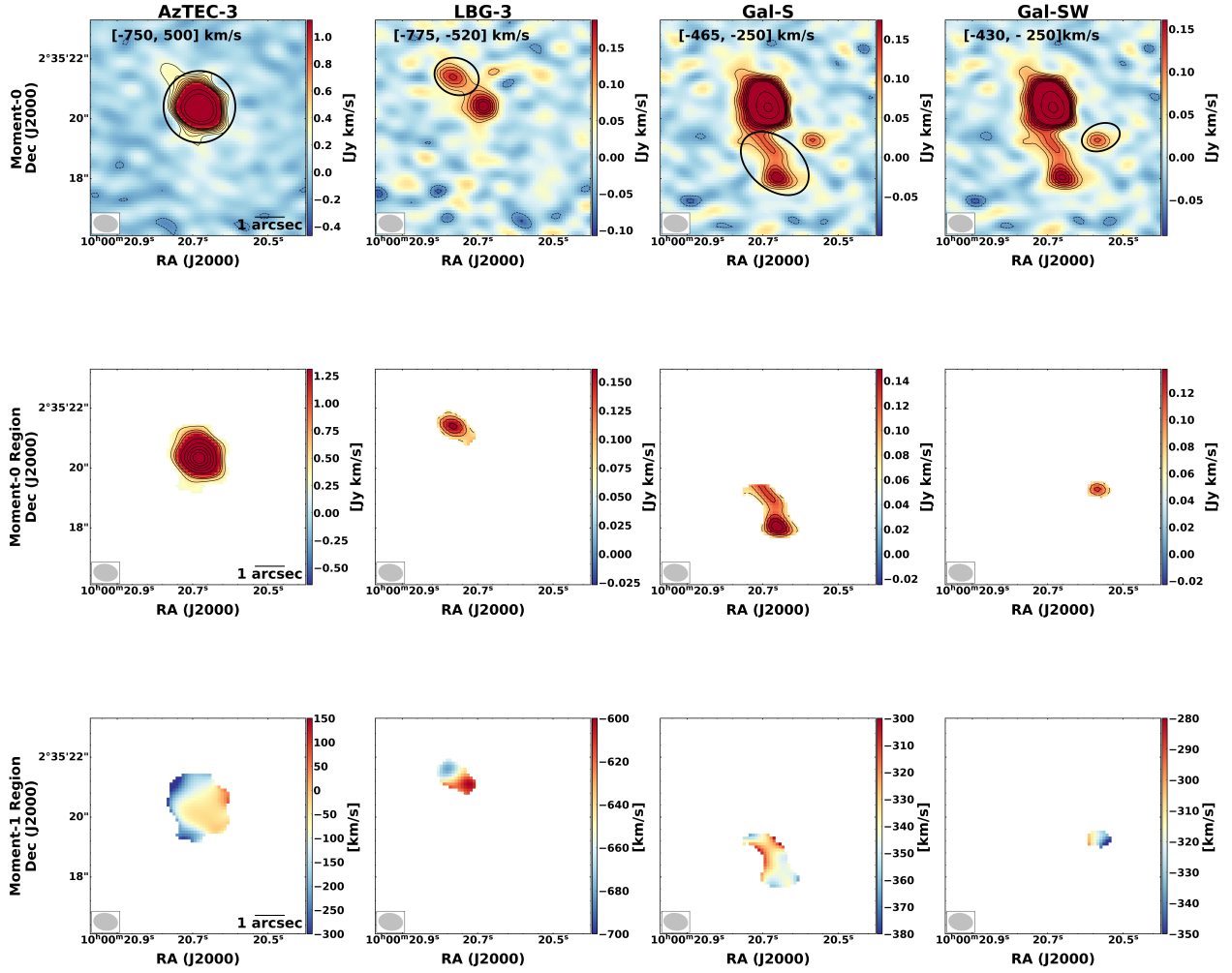


**Fig. 7.** Moment-0 and moment-1 maps for AzTEC-3 system. The top row shows moment-0 maps of the original [C II] and the central row shows the moment-0 map of the region from which the spectra were extracted and are centered at the respective redshifts of the sources. The bottom row shows the moment-1 maps from each using the same region that the spectra were extracted from. The contours in the first panel for AzTEC-3 are shown at  $-3$ ,  $-2$ ,  $10$ ,  $20$ ,  $30$ ,  $40$ ,  $50$ , and  $60\sigma$  levels, and the contours shown in subsequent panels are at  $-3$ ,  $-2$ ,  $3$ ,  $4$ ,  $5$ ,  $6$ , and  $7\sigma$  levels where the respective  $1\sigma$  noise level has been taken from individual moment-0 maps due to the restrictive velocity ranges (and thus differing noise levels). The black circle and ellipses in the top row show the regions from which the spectra were extracted for each source. The synthesized beam is shown in the bottom left of the images.

that this offset between the three types of emission is likely linked to spatial offset between different types of emission in this source. The offset of this emission also affects the subtraction we performed above due to the possibility that we have in fact subtracted some flux pertaining to LBG-3 that could be included in our model of the emission from AzTEC-3. Thus, we suggest that the continuum flux reported in this paper for LBG-3 be treated as a lower limit. Without additional higher resolution data, a robust conclusion about the nature of this offset is not possible.

We detect an additional continuum source at  $\sim 10.5$  significance, referred to extra source (ES), in the AzTEC-3 field at the position  $10:00:21.066$ ,  $+02:35:16.975$ , which is shown in Fig. 5. This source is bright across the HST WFC3 filters, but it is undetected in [C II] emission, indicating that it is at a different redshift. Continuum flux measurements and source size are provided in Table 5.

### 3.3.3. SED fitting

We fit the SED of AzTEC-3 using photometry extracted from HST imaging utilizing the source extraction algorithm SExtractor (Bertin & Arnouts 1996) and our ALMA photometry (see

Table 7). We matched the resolution of the HST images to the lowest resolution filter; we note that the companion sources are not blended with the emission from AzTEC-3 in the HST imaging. We fit the SED using Bagpipes (Carnall et al. 2018), assuming a constant star formation history, a Calzetti reddening law to describe the dust attenuation, and a Chabrier initial mass function (IMF, Chabrier 2003). The mass of the central source was allowed to vary from  $10^8$ – $10^{14} M_{\odot}$ , and the metallicity was allowed to vary from  $0.01$ – $1.0 Z_{\odot}$ . We used the SED fit from Bagpipes to calculate the  $L_{\text{IR}}$  (integrated from  $8$ – $1000 \mu\text{m}$ ) of AzTEC-3, which is subsequently utilized below in determination of the SMG’s properties.

## 4. Discussion

### 4.1. Magnetic fields

The mechanisms for the predicted polarization of the [C II] fine structure line has been named ground state alignment (GSA; Yan & Lazarian 2006, 2012; Zhang et al. 2015). GSA occurs due to the interaction of an anisotropic radiation field with atoms or ions with fine- or hyperfine-structures. A magnetic field induces precession, which causes the atom or ion to align with the mag-



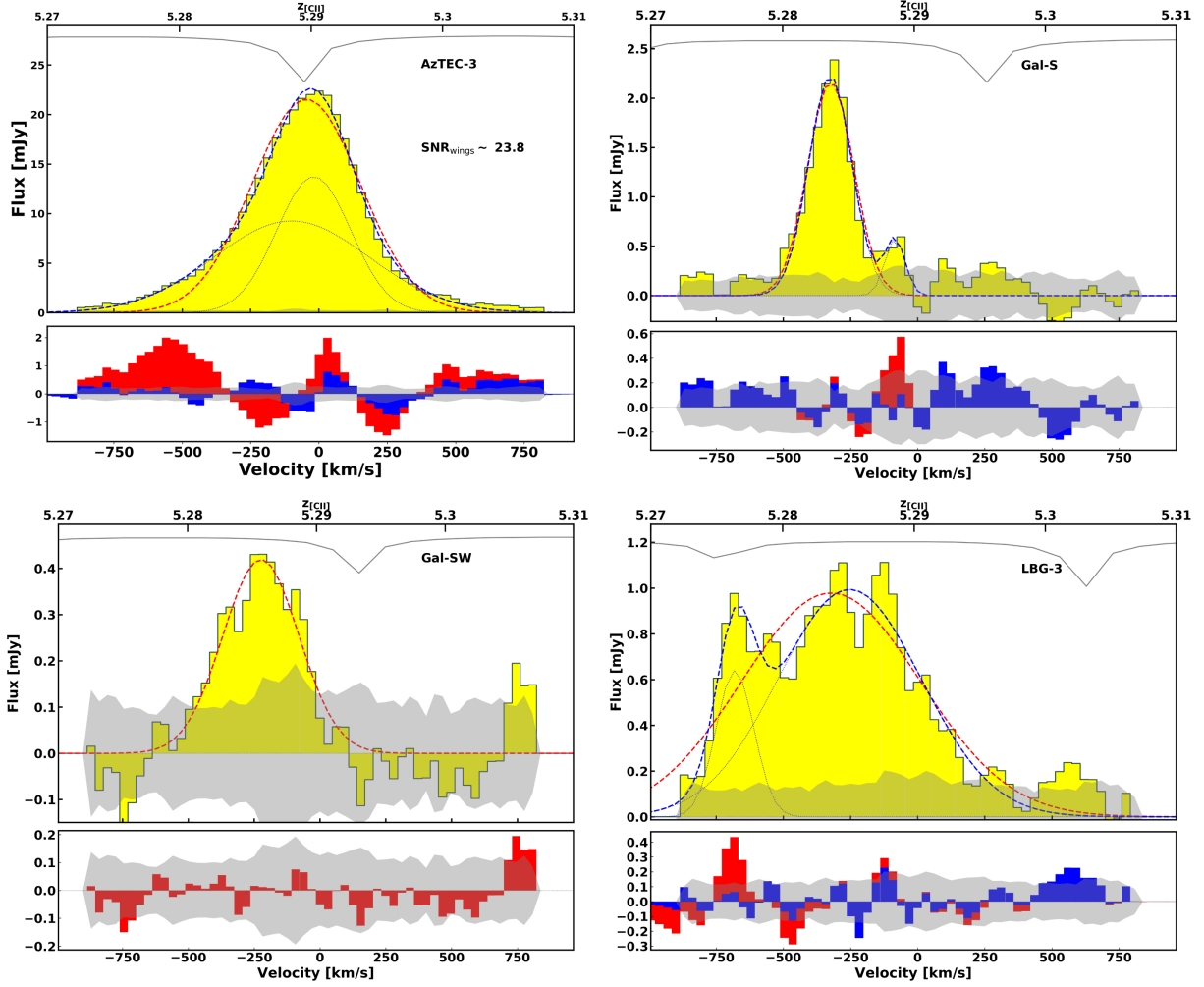


**Fig. 8.** Spectra for the AzTEC-3 system. The red line shows the single Gaussian fit to the data, and the blue line shows the double Gaussian fit to the data. For AzTEC-3, the blue wing  $< -500 \text{ km s}^{-1}$  is significantly more prominent than the red wing. We fit LBG-3 and Gal-SW with double Gaussians to account for the additional “bumps” in the spectra (most obvious in LBG-3), which are likely blended flux from the SMG. The atmospheric transmission is shown as a gray line in the top subplot for every source.

**Table 7.** Photometry for AzTEC-3 extracted from HST images using SExtractor.

Filter	Magnitude [mag <sub>AB</sub> ]
<i>F</i> 606W	$28.89 \pm 0.30$
<i>F</i> 814W	$27.17 \pm 0.10$
<i>F</i> 105W	$24.92 \pm 0.03$
<i>F</i> 125W	$24.68 \pm 0.02$
<i>F</i> 160W	$24.52 \pm 0.02$

netic field. As a result, the emission or absorption of the spectral lines becomes polarized and the polarization direction reflects the direction of the magnetic field. The atoms align predominantly at their ground state level. Due to the low emission and absorption rates involved in these transitions, and hence their long life spans, already weak fields ( $B > 10^{-15} \text{ G}$ ) can cause alignment.

Predictions for the level of [C II] polarization based on the GSA effect have been made for [C II] emission near galactic star-forming regions (Zhang & Yan 2018). Near the strong

anisotropic radiation field produced from the regions, [C II] polarization up to  $\sim 30\%$  could be expected. Since the radiation field in starburst galaxies and AGN hosts are similarly energetic, comparable levels of polarization could have been expected in early star-forming galaxies and AGNs (Zhang & Yan 2018). Our observations do not reveal any linear polarization of [C II] with  $3\sigma$  limits to the polarization percentages at the peak of emission  $< 5\%$  and for the integrated emission  $< 1\%$ .

There are two possible explanations for such low or non-existent levels of polarization. Firstly, the GSA prediction might not be relevant in conditions where the [C II] emission originates in the observed SMG and quasar, because the anisotropic radiation field is not sufficient to cause significant polarization. Alternatively, if the magnetic field is sufficiently irregular or has a large turbulent component within our resolution elements, beam depolarization will reduce the polarization fraction. Our angular resolution corresponds to  $\sim 3.1 \text{ kpc}$  and  $\sim 4.7 \text{ kpc}$  for BRI0952 and AzTEC-3, respectively. These scales are not significantly larger than those where structured fields are observed in nearby galaxies (e.g., Beck 2015; Lopez-Rodriguez et al. 2021), but if the magnetic field follows spiral arms or warped disks, like in the case of Centaurus A (Lopez-Rodriguez 2021), depolarization could still be large. Without a better estimate of the expected linear polarization fraction in SMGs and around quasars, we

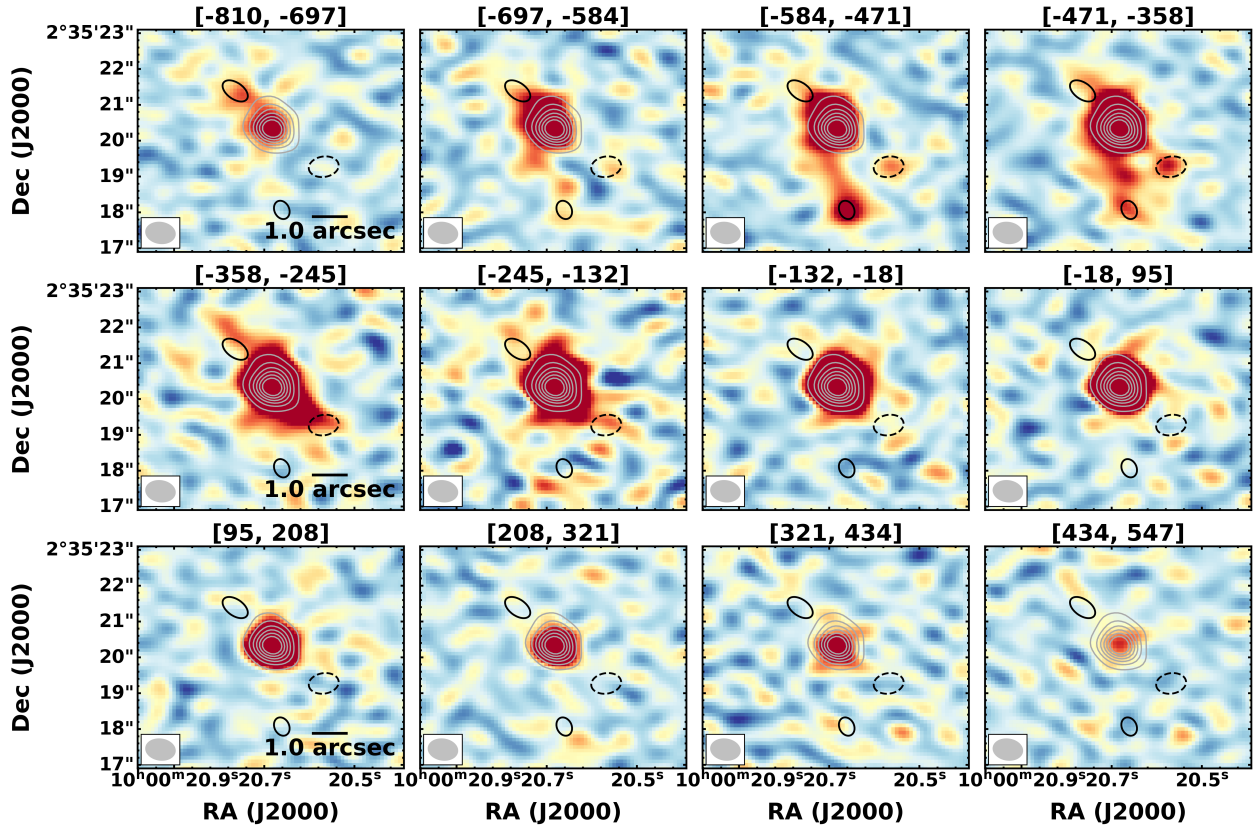


**Fig. 9.** Velocity maps of AzTEC-3 showing [C II] emission across the velocity range of the line. The velocity range is provided at the top of the images. The gray contours are at 10, 20, 30, 40, 50, and 60 $\sigma$  levels from the moment-0 map of AzTEC-3, which is shown in Fig. 7. The black ellipses indicate the positions and sizes of the three companions from CASA’s IMFIT routine where the dashed ellipse around Gal-SW denotes an upper-limit point source. The “gas-bridge” structure between AzTEC-3 and Gal-S is seen in the velocity range of  $-584$  to  $-358$  km s $^{-1}$ . The size of the synthesized beam is shown in the bottom left corner of the images.

cannot use our limits to provide meaningful constraints on the level of depolarization, and thus the level of structure in the magnetic field. However, unless the GSA mechanism is much less effective than expected, it appears unlikely that a strong ordered magnetic field exists at the kiloparsec scale in the two sources in this paper.

#### 4.2. Infrared luminosity

We obtain an  $L_{\text{IR}}$  estimate for AzTEC-3 by integrating our SED from Bagpipes from 8–1000  $\mu\text{m}$  of  $L_{\text{IR}} = (7.3 \pm 0.2) \times 10^{13} L_{\odot}$ . Although the central source is blended with surrounding companions, we anticipate that the uncertainty caused by the companion’s IR luminosity will be small and we do not add additional errors to the  $L_{\text{IR}}$  of AzTEC-3. This value is consistent with that reported by Capak et al. (2011), as they provide a wide range of possible  $L_{\text{IR}}$  values ranging from  $(2.2\text{--}11) \times 10^{13} L_{\odot}$  for the 8–1000  $\mu\text{m}$  wavelength range. Riechers et al. (2014) reported a  $L_{\text{FIR}}$  that is a factor of  $\sim 6.5$  times lower than our reported  $L_{\text{IR}}$ , which is outside the range of error typically ascribed to differences between  $L_{\text{IR}}$  and  $L_{\text{FIR}}$ <sup>7</sup> (Carilli & Walter 2013). We suggest that discrepancies between these two reported values, apart from the utilized wavelength range, derive from the number of data points used for each fit. Riechers et al. (2014) used a higher number of data points than in our SED fitting; however,

both analyses lack IR coverage, making it difficult to obtain high levels of accuracy, and thus  $L_{\text{FIR}}$  or  $L_{\text{IR}}$ , from the SED fit.

To determine a lower limit on the IR luminosity of the companions of AzTEC-3, we used a modified blackbody approximation (e.g., Knudsen et al. 2003, Eq. (2)), assuming a temperature of 45 K and  $\beta = 1.7$  (typical values for high-redshift sources; Beelen et al. 2006; Dunne et al. 2011; Carniani et al. 2019). We utilized this approach rather than an SED fit as the SED of the companions is poorly sampled, especially in the far-IR, and the accuracy of sub-mm photometry is affected by the blending of the continuum emission from the central SMG. Calculated lower limits are provided in Table 6.

A similar fit for the IR luminosity was performed for BRI0952, integrating the SED between 8 and 1000  $\mu\text{m}$ . We assume the same approximation as for AzTEC-3: the effect of the companion sources on the SED and  $L_{\text{IR}}$  will be negligible due to their faintness in comparison to the quasar. Specifically, we find that the IR luminosity due to star formation is  $L_{\text{IRSF}} = (7.66 \pm 2.49) \times 10^{12} L_{\odot}$  and the IR luminosity due to AGN is  $L_{\text{IRAGN}} = (2.23 \pm 0.72) \times 10^{14} L_{\odot}$ . We note that the error on the IR luminosity comes from the uncertainty on the lensing factor. We find that  $L_{\text{IRSF}}$  is a factor of  $\sim 5$  higher than that reported by Gallerani et al. (2012). We suggest that this is for two main reasons: (i) the methodology used for fitting – Gallerani et al. (2012) scaled a template SED to the 870  $\mu\text{m}$  continuum flux, while our model fits based on a number of photometric values, increasing the accuracy of the fit – and (ii) the wavelength range used in fitting (the range 42–122  $\mu\text{m}$  is used in Gallerani et al. 2012).

<sup>7</sup> In this analysis, we assume  $L_{\text{FIR}} \sim 0.75 \times L_{\text{IR}}$ , following Decarli et al. (2017).

#### 4.3. Star-formation rate

We calculated the SFR of BRI0952 and AzTEC-3, along with their surrounding sources, using different methods. By assuming a Chabrier IMF we can infer the SFR of each source via the following relation:  $\text{SFR} \sim 10^{-10} L_{\text{IR}}$ , where  $L_{\text{IR}}$  is given in  $L_{\odot}$  (Carilli & Walter 2013). This yields an SFR of  $770 M_{\odot} \text{ yr}^{-1}$  for the quasar BRI0952 using  $L_{\text{IR, SF}}$  and  $\sim 7340 M_{\odot} \text{ yr}^{-1}$  for AzTEC-3 (significantly higher than that reported by Riechers et al. 2014 of  $1100 M_{\odot} \text{ yr}^{-1}$ ).

These extremely high values are similar to those reported for other peculiar sources in the high-redshift universe. Daddi et al. (2009) reported an SFR of  $>1000 M_{\odot} \text{ yr}^{-1}$  in the SMGs GN20 and GN20.2 and notes that there is no evidence of AGN activity. Similarly, SFRs of  $\geq 1000 M_{\odot} \text{ yr}^{-1}$  have been reported in HDF850.1 (Walter et al. 2012), AzTEC-1 (Yun et al. 2015; Sharda et al. 2019), HFLS3 (Robson et al. 2014; Cooray et al. 2014), and BRI1202 (Carilli et al. 2013).

Following the same procedure we infer the SFRs of the companions of AzTEC-3 from the modified blackbody  $L_{\text{IR}}$  fit, reported in Table 6. The companions exhibit significantly lower SFRs than AzTEC-3, although we assume that these values provide a lower limit for the companions. We find comparable SFRs to those reported for the quasar companions in Neeleman et al. (2019).

We derive SFRs through an additional method using the [C II]-SFR relation for starburst galaxies from De Looze et al. (2014), provided in Sect. 3.2.2, which are given in Table 6. This results in a similar distribution to the above method, demonstrating the significant discrepancy between the SFR of the companions and that of the central sources in both fields.

We caution that using [C II] as a means of inferring SFR may be inaccurate as the [C II] emission is likely tracing other processes in addition to star formation within the galaxies. The [C II] emission could be tracing more extreme processes or neutral gas (Pavesi et al. 2018) within the galaxy. If this is the case in AzTEC-3 or BRI0952, this could also contaminate the measurement of the SFR from the [C II] emission. We further note the degeneracy inherently present in determining a SFR from a galaxy's [C II] luminosity due to the [C II] versus FIR deficit, which is explored below.

#### 4.4. [C II] deficit

The [C II] line is well known to exhibit a deficit with increasing IR luminosity (e.g., Díaz-Santos et al. 2013, 2017; Gullberg et al. 2015, 2018; Lagache et al. 2018). This has been heavily investigated at high redshift (e.g., Stacey et al. 2010; Wang et al. 2013; Gullberg et al. 2015, 2018; Decarli et al. 2017; Lagache et al. 2018; Neeleman et al. 2019), with many proposed explanations including the physical scale of star formation, [C II] saturation, optical depth effects, increased dust grain charge in PDRs and the ISM, and AGN activity (Casey et al. 2014). Some studies at high redshift have suggested that the lowest ratios occur preferentially in AGN host galaxies (Stacey et al. 2010). This may not be exclusively limited to [C II] emission, as other fine structure lines such as [O I], [O III], [N II], and [N III] have been found to exhibit this deficit as well (e.g., Graciá-Carpio et al. 2011; Decarli et al. 2012; Farrah et al. 2013). We plot the  $L_{\text{[C II]}}/L_{\text{IR}}$  ratios as a function of the IR luminosity for the sources in our sample, as well as other low- and high-redshift galaxies in Fig. 10. The ratios we find for BRI0952 and AzTEC-3 are similar to those found in HFLS3

(Riechers et al. 2013) and the ratios reported for two of the four quasars studied in Decarli et al. (2017).

For the companion galaxies, we also investigated the  $L_{\text{[C II]}}/L_{\text{IR}}$  ratio, though we note that the errors are very large due to the additional uncertainty caused by the deblending of emission from the central bright source. As the IR luminosity is seen as a lower limit (see Sect. 4.2), the ratio can be treated as an upper limit. The resulting values are consistent with those of local star-forming galaxies (Díaz-Santos et al. 2013) and are higher than those reported for high-redshift companion sources detected in [C II] (e.g., Carilli et al. 2013; Decarli et al. 2017; Neeleman et al. 2019).

A possible explanation for the ratios observed in AzTEC-3 and BRI0952 is that of [C II] saturation (e.g., Muñoz & Oh 2016; Gullberg et al. 2018). These sources are both hosts to extreme star formation and, in the case of BRI0952, AGN activity. If the temperatures in the majority of the environments in which [C II] is produced exceed the ground state temperature (92 K), we can expect this line to saturate and other fine structure lines to become the primary coolants of the ISM. If this is the case for these two sources, it could explain the deficits observed in both. Observations of other fine structure lines in these sources could provide further clues to the origin of the deficit.

#### 4.5. Outflows and turbulence

As shown in Sects. 3.3.1 and 3.2.2, the [C II] emission line profiles of the bright target sources, namely BRI0952 and AzTEC-3, are better fit when including an additional broad Gaussian function. The presence of broad, higher velocity wings in the line profiles are often interpreted as an indication of high-velocity outflows. We note that this need not be a unique interpretation; however, as this is a common analysis that has been done in many previous works (e.g., Feruglio et al. 2010; Aalto et al. 2012; Maiolino et al. 2012; Ciccone et al. 2014, 2015; Gallerani et al. 2018; Bischetti et al. 2019; Stanley et al. 2019; Ginolfi et al. 2020). We pursue this below.

We used the luminosity of the broad component of the [C II] line in both AzTEC-3 and BRI0952 to infer a mass outflow rate using the equation from Hailey-Dunsheath et al. (2010) to calculate the mass of the outflow. Similarly to the method employed by Maiolino et al. (2012), Ciccone et al. (2015), and Stanley et al. (2019), we assumed  $X_{\text{C}^+} = 1.4 \times 10^{-4}$ ,  $T = 200 \text{ K}$ , and  $n \gg n_{\text{crit}}$  – typical values for PDRs. We estimated the velocity of the outflow by assuming a constant outflow rate of  $v_{\text{out}} = 0.5 \times FWHM_{\text{broad}}$  over a region with a radius of  $R_{\text{out}}$ , allowing us to calculate the outflow rate using  $\dot{M}_{\text{out}} = M_{\text{out}} \times v_{\text{out}}/R_{\text{out}}$ .

We determined the outflow radius as the major axis of the extent of the [C II] emission for AzTEC-3 ( $\sim 7.5 \text{ kpc}$ ) and BRI0952 ( $\sim 2.3 \text{ kpc}$ ); for BRI0952, this measurement was taken using the major axis through both the image plane top and bottom images combined, and corrected for lensing magnification<sup>8</sup>. We investigated alternative methods for determining the mass outflow rate below. We find outflow rates of  $\dot{M}_{\text{out}} = 238 \pm 30 M_{\odot} \text{ yr}^{-1}$  for AzTEC-3 and  $\dot{M}_{\text{out}} = 98 \pm 19 M_{\odot} \text{ yr}^{-1}$  for BRI0952. Although these values are lower than those found for other individual detections of quasar-driven outflows (assumed to be the case for BRI0952; e.g., Feruglio et al. 2010, 2015; Sturm et al. 2011; Cano-Díaz et al. 2012; Maiolino et al. 2012; Ciccone et al. 2014), they are in good agreement with outflow rates estimates through stacking analyses (e.g., Gallerani et al. 2018; Stanley et al. 2019; Ginolfi et al. 2020). The latter samples

<sup>8</sup> The lensing magnification factor we utilized to correct the extent was  $\mu = 3$ .



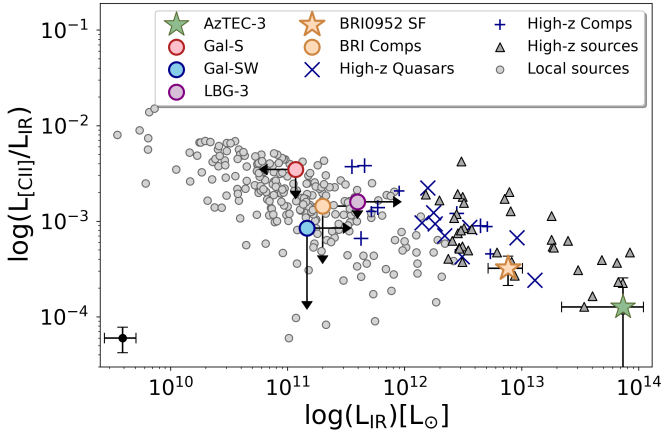


**Fig. 10.**  $L_{\text{[CII]}}/L_{\text{IR}}$  ratio as a function of  $L_{\text{IR}}$  for local and high-redshift sources. Local ( $z < 1$ ) sources are taken from Díaz-Santos et al. (2013). High-redshift sources are from De Looze et al. (2014) and Gullberg et al. (2015). Literature results for high-redshift quasars and companion sources are taken from Decarli et al. (2017) and Neeleman et al. (2019, for these we take an average of the reported  $L_{\text{IR}}$ ). We note that we only consider the  $L_{\text{[CII]}}/L_{\text{IR}}$  as an upper limit for all companion sources. The error bar we used for BRI0952 comes from the uncertainty on the lensing factor on  $L_{\text{IR}}$ . The error bar on the  $L_{\text{IR}}$  and hence  $L_{\text{[CII]}}/L_{\text{IR}}$  ratio of AzTEC-3 is taken to be the range of  $L_{\text{IR}}$  values provided by Capak et al. (2011). For data points taken from other papers, we assumed  $L_{\text{FIR}} \sim 0.75 \times L_{\text{IR}}$  (following Decarli et al. 2017), but added an additional indicative error bar to the bottom left of the plot indicating the conservative estimate  $\sim 30\%$  due to this assumption (Carilli & Walter 2013).

are comprised of more ‘normal’ high-redshift sources, so the validity of the comparison is tenuous and the methodology used is discussed at the end of this section.

As noted above, there are different methods for disentangling a potential contribution of a high-velocity outflow to the line profile, and we note that the velocity profile of the outflow need not be described by a single Gaussian. As an alternative, we determined the strength of the outflow by utilizing only the flux not accounted for in a single Gaussian fit to the [C II] emission; effectively subtracting the single component from the broad one. This yields a significantly lower mass outflow rate, which we treated as a lower limit for BRI0952 and AzTEC-3. Using this method, we find mass outflow rates of  $28 \pm 8 M_{\odot} \text{ yr}^{-1}$  for AzTEC-3 and  $12 \pm 4 M_{\odot} \text{ yr}^{-1}$  for BRI0952. We attribute the discrepancy between the two methods, at least in part, to be the effect of the companion sources on the [C II] line emission profile. If the emission from the central source is blended with that of the companions, it is possible that the double-Gaussian fit (and thus the broad complex emission line profiles) are simply an artifact caused by this blending.

We caution that the differential lensing of the quasar may be contributing to the high-velocity wings. To this end, for an additional investigation into the mass outflow rate of BRI0952 we used the spectra extracted from Img-N (as mentioned in Sect. 3.2.2 and shown in Fig. 3). We use a radius of  $0.35''$  ( $\sim 2.38$  kpc), corrected using the same lensing factor as described above),  $FWHM_{\text{broad}} = 543 \text{ km s}^{-1}$ , and  $L_{\text{[CII]broad}} = 0.22 \times 10^9 L_{\odot}$ , resulting in an outflow of  $\dot{M}_{\text{out}} = 74 \pm 19 M_{\odot} \text{ yr}^{-1}$ . The exact impact of the gravitational lensing, and in particular differential lensing, is challenging to estimate, and further modeling based on higher resolution and higher sensitivity data across multiple wavelengths would be needed. We note that systematic errors on the mass outflow rate estimates, along with the systematic errors

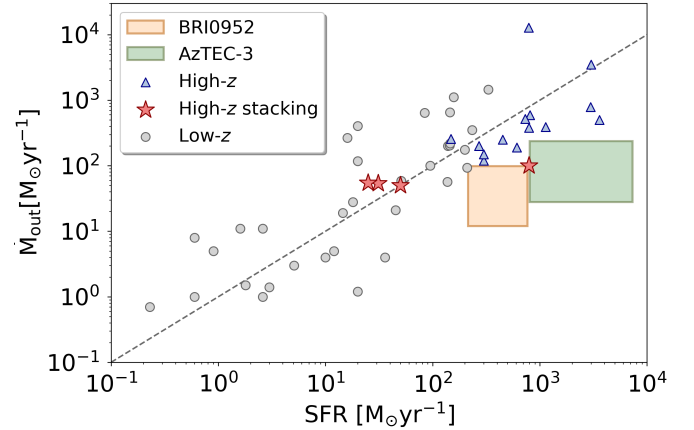


**Fig. 11.** Mass outflow rate versus SFR for our objects and low- and high-redshift galaxies, including stacking approaches at high redshift. The green and orange rectangles represent the range of possible values for AzTEC-3 and BRI0952, respectively. The low- $z$  comparison sample is taken from Fluetsch et al. (2019), high-redshift direct observations are taken from Maiolino et al. (2012), George et al. (2014), Feruglio et al. (2017), Brusa et al. (2018), Herrera-Camus et al. (2019), Jones et al. (2019), Spilker et al. (2020), Butler et al. (2021), and high-redshift stacking averages are taken from Gallerani et al. (2018), Bischetti et al. (2019), Ginolfi et al. (2020). For Ginolfi et al. (2020), we plot the high-SFR sample and the median-SFR sample in their stacking methodology as separate points. We utilized an average of the mass outflow rates if a range is provided for an object.

on other quantities used for comparison (e.g., SFR), are likely to dominate over the effect of the differential lensing. An additional important consideration is the origin of this broad component, which we interpret as an outflow above; for example, we ask ourselves whether the broad component is tracing high-velocity gas outflowing from AzTEC-3 or an interaction between the SMG and the companion Gal-S. This is further discussed in Sect. 4.6.

We show the mass outflow rate estimates as a function of SFR in Fig. 11, together with similar estimates for low- and high-redshift sources. With star-formation-rate estimates that are  $\sim$  or  $> 1000 M_{\odot} \text{ yr}^{-1}$  for both BRI0952 and AzTEC-3, both sources are seen in a similar region to other results for high-redshift galaxies. For both sources, the mass outflow rate estimates are on the lower side of the average; however, we note that the large uncertainties in the  $\dot{M}_{\text{out}}$  and SFR do not allow for additional interpretation.

Outflows are generally studied through different probes, including both emission from high-velocity outflows as well as absorption line studies. In terms of high-velocity outflows, detections have been published using different lines, including CO, [C II], and [O III] $\lambda 5007$  at low and high redshift (e.g., Ciccone et al. 2014, 2015; Carniani et al. 2016; Brusa et al. 2018). So far, only a few robust detections from single  $z > 4$  quasars using [C II] have been published (Maiolino et al. 2012; Carilli et al. 2013). Studies using stacking analyses for larger samples of  $z \sim 6$  quasars provide conflicting results (e.g., Decarli et al. 2018; Stanley et al. 2019; Bischetti et al. 2019), ranging from non-detection to claimed detections. In terms of star-forming galaxies, stacking of [C II] for  $z = 4-6$  galaxies in the ALPINE survey revealed a high-velocity outflow component, finding mass outflow rates that are consistent with our results (e.g., Ginolfi et al. 2020). The use of broad [C II] emission as a means of detecting outflows was called into question by Spilker et al. (2020) following their non-detection of broad wings associated with a sample of dusty star-forming galaxies



with clear OH outflow absorption features. It is thus possible that the broad wings we detect are dominated by emission from the companion sources around AzTEC-3 and BRI0952, where the latter could also be affected by differential lensing magnification. In addition, recent studies have reexamined previous results, indicating the need for a broad component in the fitting of [C II] spectra and found these components superfluous (e.g., Meyer et al. 2022); therefore, we caution that the true nature of the broad component cannot be confirmed as an outflow in BRI0952 and AzTEC-3 without additional outflow tracers detected in these galaxies.

#### 4.6. Environment

The impact of the environment in which massive galaxies evolve at high-redshift remains an open question. These two systems present extreme situations in which to study the effects of faint companion sources in the early universe.

The AzTEC-3 system, with the presence of multiple close companions, detected either in [C II] or in optical or continuum observations, provide an exceptional laboratory to study the effect of close companions near intense starbursts in the early Universe. There are three companion galaxies within a projected distance of  $\sim 18$  kpc from the central SMG, and an additional system of possibly merging galaxies located at a projected distance of  $\sim 95$  kpc from the central source (Riechers et al. 2014), though the latter is not covered by our observations. We detect a bridge-like structure between the companion galaxy Gal-S and AzTEC-3, suggesting the possible occurrence of a gas-exchange between the two galaxies extending over  $\sim 12$  kpc. This “gas bridge” between Gal-S and AzTEC-3 is very similar to that observed by Díaz-Santos et al. (2018) between the Hot DOG W2246 and a companion, although only about half as large in spatial extent. Further investigation of this requires higher resolution ALMA data and an improved method for isolating and subtracting the emission from the central source. As mentioned in Sect. 3.3, we detect a velocity gradient between LBG-3 and AzTEC-3, indicating an additional possible interaction. The detections of Lyman- $\alpha$  between these two galaxies in Guaita et al. (2022) also indicate an interacting system.

In the field of BRI0952, Comp-N and Comp-SW are detected in [C II] with no further sources detected out to a projected distance of 62 kpc (corresponding to the radius of the primary beam). Also, no additional companions are seen at other wavelengths, most notably the archival HST data. Due to the non-detection of the companions in current HST and *Herschel* imaging, an analysis of comparable level to that of AzTEC-3 is currently not feasible. We note the possibility that one or both of Comp-N and Comp-SW could be in the process of merging with BRI0952. If this is the case, it may suggest that we are observing the quasar in a post-starburst state in which recent galaxy interactions and ongoing mergers have triggered extreme star formation and AGN activity. In order to investigate this possibility, higher-resolution data of multiple emission lines combined with a robust source plane reconstruction would be needed; this is beyond the scope of this paper. For the BRI0952 companion sources, we see no clear signs of gas-bridge-like structures (as were seen for the AzTEC-3 companion galaxies). We also note that an alternative interpretation of either of the companions Comp-N and Comp-SW could be that they represent an extended substructure in the gas distribution. If that is the case, it would likely indicate the presence of merger activity, as the gravitational forces from minor or major merger interactions could

cause a more complex gas distribution (e.g., König et al. 2014, 2018; Harada et al. 2018; Young et al. 2021).

These two systems seem to be examples of long-sought-after, theorized, typical, over-dense environments of massive sources with numerous faint companions in the high-redshift Universe. The companion sources of both systems contribute less than 10% to the total [C II] emission, and even less to the total IR luminosity between 8 and 1000  $\mu\text{m}$ . Other systems observed in recent years have also been found to have companion sources; however, most of these companions have luminosities comparable to that of the central SMG or quasar host galaxy (e.g., Clements et al. 2009; Carilli et al. 2013; Robson et al. 2014; Fogasy et al. 2017; Trakhtenbrot et al. 2017; Wardlow et al. 2018; Díaz-Santos et al. 2018; Neeleman et al. 2019; Fogasy et al. 2021; Bischetti et al. 2021). The detection of faint companion sources in these two fields, together with the results of W2246–0526 and BRI1202–0725 (Carilli et al. 2013; Díaz-Santos et al. 2018) and other such systems, are increasing the sample enabling investigation of the role of less massive companion sources on massive galaxy evolution.

Theoretical predictions from semi-analytical model simulations suggest that 22% of quasars should have at least one companion galaxy with stellar masses  $>10^8 M_\odot$  (Fogasy et al. 2017). Additionally, studies show that minor mergers, especially in the high-redshift Universe, are common. Kaviraj et al. (2015) utilized the Horizon-AGN hydrodynamical cosmological simulation to show that by  $z \sim 1$  all massive galaxies ( $>10^{10} M_\odot$ ) have undergone a major or minor merger, and that minor mergers (those with a mass ratio  $>4:1$ ) are around  $2.5\times$  more frequent than major mergers between  $1 < z < 4$ . Their work also suggests that major mergers are not the dominant source of star-formation enhancement at high redshift (see Fig. 5 in Kaviraj et al. 2015). This is indicative of the need for minor mergers as fuel providers for high-redshift galaxies and is especially important for extreme SMGs hosting maximum starbursts such as AzTEC-3. The lack of current detections of smaller companion sources is likely due, in part, to the long integration time required to observe them.

In order to categorize these systems as possible minor mergers (be it progenitors or ongoing processes), we calculated the mass of the central source using a virial mass estimator following the procedure used by Riechers et al. (2014). We find the dynamical mass inferred from the [C II] emission to be  $\sim 6.5 \times 10^{10} M_\odot$  for AzTEC-3 and  $\sim 0.90 \times 10^{10} M_\odot$  for BRI0952 (lensing corrected). We used the same method to compute the masses of the companions, reported in Table 6. In the AzTEC-3 system, we find that the companions have dynamical masses of  $\leq 4\times$  that of AzTEC-3. This would classify these companions as minor mergers should they interact with the central source; we already observe signs of this for AzTEC-3 and its companions in the form of the gas bridge between these objects. These companion sources are significantly less massive than those reported by Neeleman et al. (2019). For the companions of BRI0952 we find the companions have masses  $\sim 1.5\text{--}2\times$  smaller than that of the quasar. These values for the companions are closer to the values found for the quasar companions in Neeleman et al. (2019). We note that the companion masses are likely overestimated as we do not correct for lensing along the major axis of the companions used for the virial mass estimates due to uncertainties in our lensing model, and therefore the above estimate can be seen as an upper limit.

The effect of the companions on massive sources remains to be seen. If these faint companions are dynamically interacting in some manner, such as providing gas to the central sources, this could supply the needed materials for the extreme star

formation occurring in these systems. Additionally, as suggested by McGreer et al. (2014), the possibility of mergers occurring on a relatively fast timescale as a short transitional phase could drastically limit our ability to obtain high number density observations of similar systems. We further suggest that the increased resolution now possible with ALMA will allow for increased detections of SMG and quasar systems with numerous and faint surrounding objects.

## 5. Conclusions

In this paper, we present observational results of [C II] emission from BRI0952 and AzTEC-3, along with respective companion sources. Our results lend credibility to the paradigm of major and minor mergers in the early Universe as progenitors for the massive galaxies we see in studies of the local Universe. We summarize our conclusions below.

1. We detect [C II] emission in the lensed quasar BRI0952 at  $z \sim 4.433$  and the SMG AzTEC-3 at  $z \sim 5.3$ . We report serendipitous detections of [C II] emission from two previously unreported companion sources around BRI0952 and new detections of [C II] emission from three companions surrounding AzTEC-3. These companions are each located within  $3''$  (18 kpc) of the central source.
2. We present a full-polarization analysis of the [C II] emission lines for both main targets. No polarization was detected, and upper limits are provided. The results suggest that strong ordered magnetic fields are unlikely to exist at the kiloparsec scale in the two studied sources, unless ground state alignment is a less effective mechanism than expected.
3. We constructed a new lensing model for BRI0952 using VISILENS (Spilker et al. 2016), yielding a lensing magnification factor of  $\mu \sim 4$  for the quasar and insignificant lensing magnification of the two companion sources. Our model suggests that differential lensing is occurring across the surface of BRI0952 in both [C II] and continuum emission. This difference is likely insubstantial (or within errors) for our purposes, but it is important to keep it in mind when considering the physical properties of the lensed images.
4. The inferred SFR from the IR luminosity of both the central SMG AzTEC-3 and the quasar BRI0952 suggest that both sources harbor starbursts of  $\sim$  or  $>1000$  solar masses per year.
5. The central SMG AzTEC-3 and a companion galaxy (Gal-S) in the field show evidence of an interlinking gas bridge. Although we do not find a strong velocity gradient across the central source, we suggest that this bridge may be indicative of an ongoing gas-exchange process or merger.
6. The [C II] line profiles for both central sources exhibit complex broad features indicating the possible presence of outflows. The mass outflow rates of both BRI0952 and AzTEC-3 are similar to results for high-redshift galaxies; any discrepancies we find are likely symptomatic of large uncertainties on both the mass outflow rate and the SFR.
7. The outflow features, combined with the observed gas-bridge structure between AzTEC-3 and its southern companion (and possibly others) and velocity-gradients between BRI0952 and companions, suggest both are interacting systems. The extent of this interaction is unknown, but if both systems are either entering or exiting a merger phase, this could explain the extreme star formation events occurring in both.

Growing evidence in recent years suggests that overdense regions leading to major and minor mergers are the progenitors of the massive galaxies we see in the local Universe. The

improved resolution possible with ALMA will allow for the increased detection of companion galaxies in high-redshift environments, allowing us to explore the credibility of mergers as means of creating the extreme SFRs observed in these objects.

**Acknowledgements.** We thank the anonymous referee for their helpful comments and insights. Kiana Kade acknowledges support from the Nordic ALMA Regional Centre (ARC) node based at Onsala Space Observatory. The Nordic ARC node is funded through Swedish Research Council grant No. 2017-00648. Kirsten Knudsen acknowledges support from the Swedish Research Council and the Knut and Alice Wallenberg Foundation. B.G. acknowledges support from the Carlsberg Foundation Research Grant CF20-0644 ‘Physical pRoperties of the InterStellar Medium in Luminous Infrared Galaxies at High redshift: PRISM-LIGHT’. Sabine König gratefully acknowledges funding from the European Research Council (ERC) under the European Union’s Horizon 2020 research and innovation programme (grant agreement No. 789410). This paper makes use of the following ALMA data: 2018.1.01536.S. ALMA is a partnership of ESO (representing its member states), NSF (USA), and NINS (Japan), together with NRC (Canada), MOST and ASIAA (Taiwan), and KASI (Republic of Korea), in cooperation with the Republic of Chile. This paper makes use of the following HST projects: 13641 (PI: Capak), 9822 (PI: COSMOS24-21), and 13384 (PI: Riechers), 8268 (PI: Impey). Based on observations made with the NASA/ESA Hubble Space Telescope, and obtained from the Hubble Legacy Archive, which is a Collaboration between the Space Telescope Science Institute (STScI/NASA), the Space Telescope European Coordinating Facility (ST-ECF/ESA) and the Canadian Astronomy Data Centre (CADC/NRC/CSA). This research made use of APLpy, an open-source plotting package for Python (Robitaille & Bressert 2012).

## References

- Aalto, S., Garcia-Burillo, S., Muller, S., et al. 2012, *A&A*, **537**, A44  
 Bañados, E., Venemans, B., Walter, F., et al. 2013, *ApJ*, **773**, 178  
 Banerji, M., Chapman, S. C., Smail, I., et al. 2011, *MNRAS*, **418**, 1071  
 Beck, R. 2015, *A&ARv*, **24**, 4  
 Beelen, A., Cox, P., Benford, D. J., et al. 2006, *ApJ*, **642**, 694  
 Beifiori, A., Courteau, S., Corsini, E. M., & Zhu, Y. 2012, *MNRAS*, **419**, 2497  
 Bennert, V. N., Treu, T., Auger, M. W., et al. 2015, *ApJ*, **809**, 20  
 Bertin, E., & Arnouts, S. 1996, *A&AS*, **117**, 393  
 Bischetti, M., Maiolino, R., Carniani, S., et al. 2019, *A&A*, **630**, A59  
 Bischetti, M., Feruglio, C., Piconcelli, E., et al. 2021, *A&A*, **645**, A33  
 Blain, A. W., Smail, I., Ivison, R. J., & Kneib, J. P. 1999, *MNRAS*, **302**, 632  
 Brusa, M., Cresci, G., Daddi, E., et al. 2018, *A&A*, **612**, A29  
 Butler, K. M., van der Werf, P. P., Rybak, M., et al. 2021, *ApJ*, **919**, 5  
 Cano-Díaz, M., Maiolino, R., Marconi, A., et al. 2012, *A&A*, **537**, L8  
 Capak, P. L., Riechers, D., Scoville, N. Z., et al. 2011, *Nature*, **470**, 233  
 Carilli, C. L., & Walter, F. 2013, *ARA&A*, **51**, 105  
 Carilli, C. L., Riechers, D., Walter, F., et al. 2013, *ApJ*, **763**, 120  
 Carnall, A. C., McLure, R. J., Dunlop, J. S., & Davé, R. 2018, *MNRAS*, **480**, 4379  
 Carniani, S., Marconi, A., Maiolino, R., et al. 2016, *A&A*, **591**, A28  
 Carniani, S., Gallerani, S., Vallini, L., et al. 2019, *MNRAS*, **489**, 3939  
 Casey, C. M., Narayanan, D., & Cooray, A. 2014, *Phys. Rep.*, **541**, 45  
 Casey, C. M., Zavala, J. A., Aravena, M., et al. 2019, *ApJ*, **887**, 55  
 Chabrier, G. 2003, *PASP*, **115**, 763  
 Chisholm, J., Tremonti, C. A., Leitherer, C., et al. 2015, *ApJ*, **811**, 149  
 Ciccone, C., Maiolino, R., Sturm, E., et al. 2014, *A&A*, **562**, A21  
 Ciccone, C., Maiolino, R., Gallerani, S., et al. 2015, *A&A*, **574**, A14  
 Clements, D. L., Petitpas, G., Farrah, D., et al. 2009, *ApJ*, **698**, L188  
 Cooray, A., Calanog, J., Wardlow, J. L., et al. 2014, *ApJ*, **790**, 40  
 Cutri, R. M., Wright, E. L., Conrow, T., et al. 2012, *VizieR Online Data Catalog*: **II/311**  
 Daddi, E., Dannerbauer, H., Stern, D., et al. 2009, *ApJ*, **694**, 1517  
 De Looze, I., Cormier, D., Lebouteiller, V., et al. 2014, *A&A*, **568**, A62  
 Decarli, R., Walter, F., Neri, R., et al. 2012, *ApJ*, **752**, 2  
 Decarli, R., Walter, F., Venemans, B. P., et al. 2017, *Nature*, **545**, 457  
 Decarli, R., Walter, F., Venemans, B. P., et al. 2018, *ApJ*, **854**, 97  
 Dekel, A., Birnboim, Y., Engel, G., et al. 2009, *Nature*, **457**, 451  
 Di Matteo, T., Springel, V., & Hernquist, L. 2005, *Nature*, **433**, 604  
 Di Matteo, T., Khandai, N., DeGraf, C., et al. 2012, *ApJ*, **745**, L29  
 Díaz-Santos, T., Armus, L., Charmandaris, V., et al. 2013, *ApJ*, **774**, 68  
 Díaz-Santos, T., Armus, L., Charmandaris, V., et al. 2017, *ApJ*, **846**, 32  
 Díaz-Santos, T., Assef, R. J., Blain, A. W., et al. 2018, *Science*, **362**, 1034  
 Dubois, Y., Devriendt, J., Slyz, A., & Teyssier, R. 2012, *MNRAS*, **420**, 2662  
 Dubois, Y., Pichon, C., Welker, C., et al. 2014, *MNRAS*, **444**, 1453

- Dunne, L., Gomez, H. L., da Cunha, E., et al. 2011, *MNRAS*, **417**, 1510
- Eigenbrod, A., Courbin, F., & Meylan, G. 2007, *A&A*, **465**, 51
- Fabian, A. C. 2012, *ARA&A*, **50**, 455
- Fan, L., Han, Y., Fang, G., et al. 2016, *ApJ*, **822**, L32
- Farrah, D., Lebouteiller, V., Spoon, H. W. W., et al. 2013, *ApJ*, **776**, 38
- Ferrarese, L., & Merritt, D. 2000, *ApJ*, **539**, L9
- Feruglio, C., Maiolino, R., Piconcelli, E., et al. 2010, *A&A*, **518**, L155
- Feruglio, C., Fiore, F., Carniani, S., et al. 2015, *A&A*, **583**, A99
- Feruglio, C., Ferrara, A., Bischetti, M., et al. 2017, *A&A*, **608**, A30
- Fluetsch, A., Maiolino, R., Carniani, S., et al. 2019, *MNRAS*, **483**, 4586
- Fogasy, J., Knudsen, K. K., Lagos, C. D. P., Drouart, G., & Gonzalez-Perez, V. 2017, *A&A*, **597**, A123
- Fogasy, J., Knudsen, K. K., Drouart, G., Lagos, C. D. P., & Fan, L. 2020, *MNRAS*, **493**, 3744
- Fogasy, J., Knudsen, K. K., Drouart, G., & Gullberg, B. 2021, *MNRAS*, **501**, 5973
- Gaia Collaboration (Brown, A. G. A., et al.) 2018, *A&A*, **616**, A1
- Gallerani, S., Neri, R., Maiolino, R., et al. 2012, *A&A*, **543**, A114
- Gallerani, S., Pallottini, A., Feruglio, C., et al. 2018, *MNRAS*, **473**, 1909
- Gebhardt, K., Bender, R., Bower, G., et al. 2000, *ApJ*, **539**, L13
- Genzel, R., Tacconi, L. J., Gracia-Carpio, J., et al. 2010, *MNRAS*, **407**, 2091
- George, R. D., Ivison, R. J., Smail, I. D., et al. 2015, *MNRAS*, **442**, 1877
- Ginolfi, M., Jones, G. C., Béthermin, M., et al. 2020, *A&A*, **633**, A90
- Graciá-Carpio, J., Sturm, E., Hailey-Dunsheath, S., et al. 2011, *ApJ*, **728**, L7
- Guaita, L., Aravena, M., Gurung-Lopez, S., et al. 2022, *A&A*, **660**, A137
- Gullberg, B., De Breuck, C., Vieira, J. D., et al. 2015, *MNRAS*, **449**, 2883
- Gullberg, B., Swinbank, A. M., Smail, I., et al. 2018, *ApJ*, **859**, 12
- Gültekin, K., Richstone, D. O., Gebhardt, K., et al. 2009, *ApJ*, **698**, 198
- Hailey-Dunsheath, S., Nikola, T., Stacey, G. J., et al. 2010, *ApJ*, **714**, L162
- Harada, N., Sakamoto, K., Martín, S., et al. 2018, *ApJ*, **855**, 49
- Häring, N., & Rix, H.-W. 2004, *ApJ*, **604**, L89
- Harrison, C. M. 2017, *Nat. Astron.*, **1**, 0165
- Heckman, T. M., Armus, L., & Miley, G. K. 1990, *ApJS*, **74**, 833
- Herrera-Camus, R., Tacconi, L., Genzel, R., et al. 2019, *ApJ*, **871**, 37
- Hopkins, P. F., Hernquist, L., Cox, T. J., & Kereš, D. 2008, *ApJS*, **175**, 356
- Hughes, D. H., Serjeant, S., Dunlop, J., et al. 1998, *Nature*, **394**, 241
- Husband, K., Bremer, M. N., Stanway, E. R., & Lehnert, M. D. 2015, *MNRAS*, **452**, 2388
- Ilbert, O., Capak, P., Salvato, M., et al. 2009, *ApJ*, **690**, 1236
- Ishibashi, W., & Fabian, A. C. 2016, *MNRAS*, **463**, 1291
- Jones, G. C., Maiolino, R., Caselli, P., & Carniani, S. 2019, *A&A*, **632**, L7
- Kaviraj, S., Cohen, S., Windhorst, R. A., et al. 2013, *MNRAS*, **429**, L40
- Kaviraj, S., Devriendt, J., Dubois, Y., et al. 2015, *MNRAS*, **452**, 2845
- Kereš, D., Katz, N., Weinberg, D. H., & Davé, R. 2005, *MNRAS*, **363**, 2
- King, A., & Pounds, K. 2015, *ARA&A*, **53**, 115
- Knudsen, K. K., van der Werf, P. P., & Jaffe, W. 2003, *A&A*, **411**, 343
- König, S., Aalto, S., Lindroos, L., et al. 2014, *A&A*, **569**, A6
- König, S., Aalto, S., Muller, S., et al. 2018, *A&A*, **615**, A122
- Kormendy, J., & Ho, L. C. 2013, *ARA&A*, **51**, 511
- Krumholz, M. R., & Dekel, A. 2010, *MNRAS*, **406**, 112
- Lagache, G., Cousin, M., & Chatzikos, M. 2018, *A&A*, **609**, A130
- Lehár, J., Falco, E. E., Kochanek, C. S., et al. 2000, *ApJ*, **536**, 584
- Litke, K. C., Marrone, D. P., Spilker, J. S., et al. 2019, *ApJ*, **870**, 80
- Lopez-Rodriguez, E. 2021, *Nat. Astron.*, **5**, 604
- Lopez-Rodriguez, E., Guerra, J., Asgari-Targhi, M., & Schmelz, J. T. 2021, *ApJ*, **914**, 24
- Madau, P., & Dickinson, M. 2014, *ARA&A*, **52**, 415
- Magorrian, J., Tremaine, S., Richstone, D., et al. 1998, *AJ*, **115**, 2285
- Maiolino, R., Caselli, P., Nagao, T., et al. 2009, *A&A*, **500**, L1
- Maiolino, R., Gallerani, S., Neri, R., et al. 2012, *MNRAS*, **425**, L66
- Mazzucchelli, C., Bañados, E., Decarli, R., et al. 2017, *ApJ*, **834**, 83
- McGreer, I. D., Fan, X., Strauss, M. A., et al. 2014, *AJ*, **148**, 73
- McMullin, J. P., Waters, B., Schiebel, D., Young, W., & Golap, K. 2007, in *Astronomical Data Analysis Software and Systems XVI*, eds. R. A. Shaw, F. Hill, & D. J. Bell, *ASP Conf. Ser.*, **376**, 127
- Meyer, R. A., Walter, F., Ciccone, C., et al. 2022, *ApJ*, **927**, 152
- Momcheva, I. G., Williams, K. A., Cool, R. J., Keeton, C. R., & Zabludoff, A. I. 2015, *ApJS*, **219**, 29
- Muñoz, J. A., & Oh, S. P. 2016, *MNRAS*, **463**, 2085
- Mullaney, J. R., Alexander, D. M., Goulding, A. D., & Hickox, R. C. 2011, *MNRAS*, **414**, 1082
- Narayanan, D., Turk, M., Feldmann, R., et al. 2015, *Nature*, **525**, 496
- Neeleman, M., Bañados, E., Walter, F., et al. 2019, *ApJ*, **882**, 10
- Oteo, I., Ivison, R. J., Dunne, L., et al. 2016, *ApJ*, **827**, 34
- Patton, D. R., Wilson, K. D., Metrow, C. J., et al. 2020, *MNRAS*, **494**, 4969
- Pavesi, R., Riechers, D. A., Sharon, C. E., et al. 2018, *ApJ*, **861**, 43
- Pearson, W. J., Wang, L., Alpaslan, M., et al. 2019, *A&A*, **631**, A51
- Reines, A. E., & Volonteri, M. 2015, *ApJ*, **813**, 82
- Riechers, D. A., Bradford, C. M., Clements, D. L., et al. 2013, *Nature*, **496**, 329
- Riechers, D. A., Carilli, C. L., Capak, P. L., et al. 2014, *ApJ*, **796**, 84
- Rieder, M., & Teyssier, R. 2017, *MNRAS*, **471**, 2674
- Robshaw, T., Quataert, E., & Heiles, C. 2008, *ApJ*, **680**, 981
- Robitaille, T. 2012, *Astrophysics Source Code Library* [record ascl:1208.017]
- Robson, E. I., Ivison, R. J., Smail, I., et al. 2014, *ApJ*, **793**, 11
- Rupke, D. S., Veilleux, S., & Sanders, D. B. 2005, *ApJ*, **632**, 751
- Sánchez-Monge, Á., Schilke, P., Ginsburg, A., Cesaroni, R., & Schmiedeke, A. 2018, *A&A*, **609**, A101
- Sharda, P., da Cunha, E., Federrath, C., et al. 2019, *MNRAS*, **487**, 4305
- Sijacki, D., Vogelsberger, M., Genel, S., et al. 2015, *MNRAS*, **452**, 575
- Smail, I., Ivison, R. J., & Blain, A. W. 1997, *ApJ*, **490**, L5
- Sparre, M., & Springel, V. 2016, *MNRAS*, **462**, 2418
- Spilker, J. S., Marrone, D. P., Aravena, M., et al. 2016, *ApJ*, **826**, 112
- Spilker, J. S., Aravena, M., Phadke, K. A., et al. 2020, *ApJ*, **905**, 86
- Stacey, G. J., Geis, N., Genzel, R., et al. 1991, *ApJ*, **373**, 423
- Stacey, G. J., Hailey-Dunsheath, S., Ferkinhoff, C., et al. 2010, *ApJ*, **724**, 957
- Stanley, F., Harrison, C. M., Alexander, D. M., et al. 2018, *MNRAS*, **478**, 3721
- Stanley, F., Jolly, J. B., König, S., & Knudsen, K. K. 2019, *A&A*, **631**, A78
- Sturm, E., González-Alfonso, E., Veilleux, S., et al. 2011, *ApJ*, **733**, L16
- Trakhtenbrot, B., Lira, P., Netzer, H., et al. 2017, *ApJ*, **836**, 8
- Venemans, B. P., Walter, F., Neeleman, M., et al. 2020, *ApJ*, **904**, 130
- Walter, F., Decarli, R., Carilli, C., et al. 2012, *Nature*, **486**, 233
- Wang, R., Wagg, J., Carilli, C. L., et al. 2013, *ApJ*, **773**, 44
- Wardlow, J. L., Simpson, J. M., Smail, I., et al. 2018, *MNRAS*, **479**, 3879
- Weiner, B. J., Coil, A. L., Prochaska, J. X., et al. 2009, *ApJ*, **692**, 187
- Willott, C. J., Percival, W. J., McLure, R. J., et al. 2005, *ApJ*, **626**, 657
- Yan, H., & Lazarian, A. 2006, *ApJ*, **653**, 1292
- Yan, H., & Lazarian, A. 2012, *J. Quant. Spectrosc. Radiat. Transf.*, **113**, 1409
- Young, L. M., Meier, D. S., Bureau, M., et al. 2021, *ApJ*, **909**, 98
- Yue, M., Fan, X., Schindler, J.-T., McGreer, I. D., & Huang, Y.-H. 2019, *ApJ*, **883**, 141
- Yun, M. S., Aretxaga, I., Gurwell, M. A., et al. 2015, *MNRAS*, **454**, 3485
- Zhang, H., & Yan, H. 2018, *MNRAS*, **475**, 2415
- Zhang, H., Yan, H., & Dong, L. 2015, *ApJ*, **804**, 142

## Appendix A: Continuum-subtracted spectra

Presented in this appendix are the figures showing the total spectra compared with the continuum-subtracted spectra for each source (see Figures A.1 and A.2).

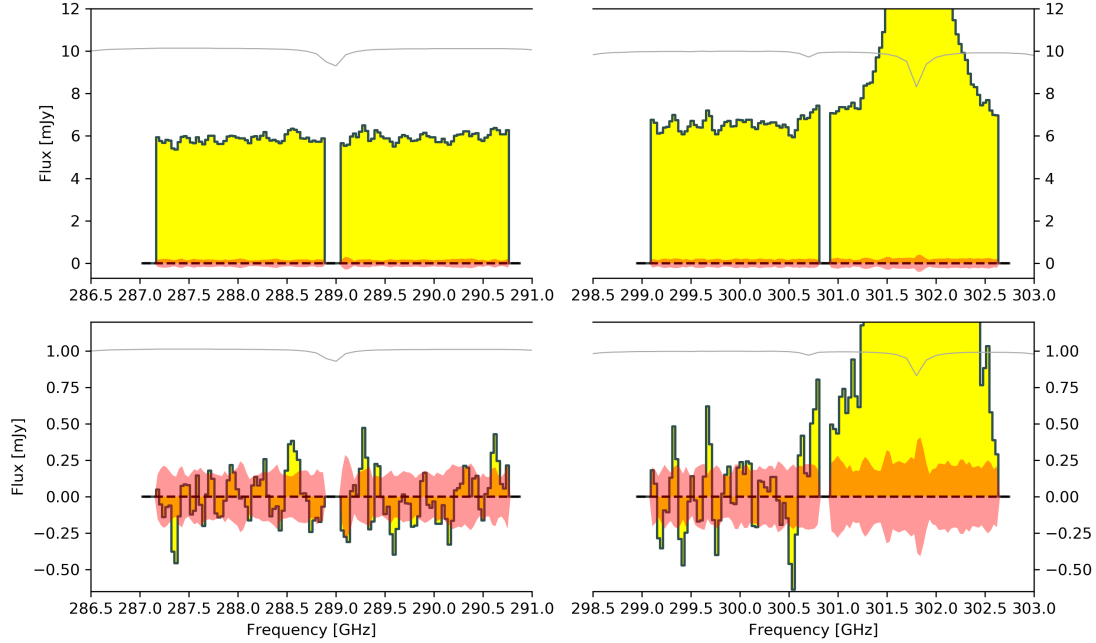


**Fig. A.1.** Pre-continuum-subtracted (top) and post-continuum-subtracted (bottom) spectra of AzTEC-3 extracted from the same region as the spectra (black circle shown in panel 1 of Figure 7 using a fit on the order of 1 and encompassing frequencies up to 300 GHz. The red region represents the  $1\sigma$  rms of the image and the gray line represents the atmospheric transmission at 1.0 mm PVW. The possible additional [C II] wing feature mentioned in Section 2 can be seen in the 300.5–301 GHz frequency range.

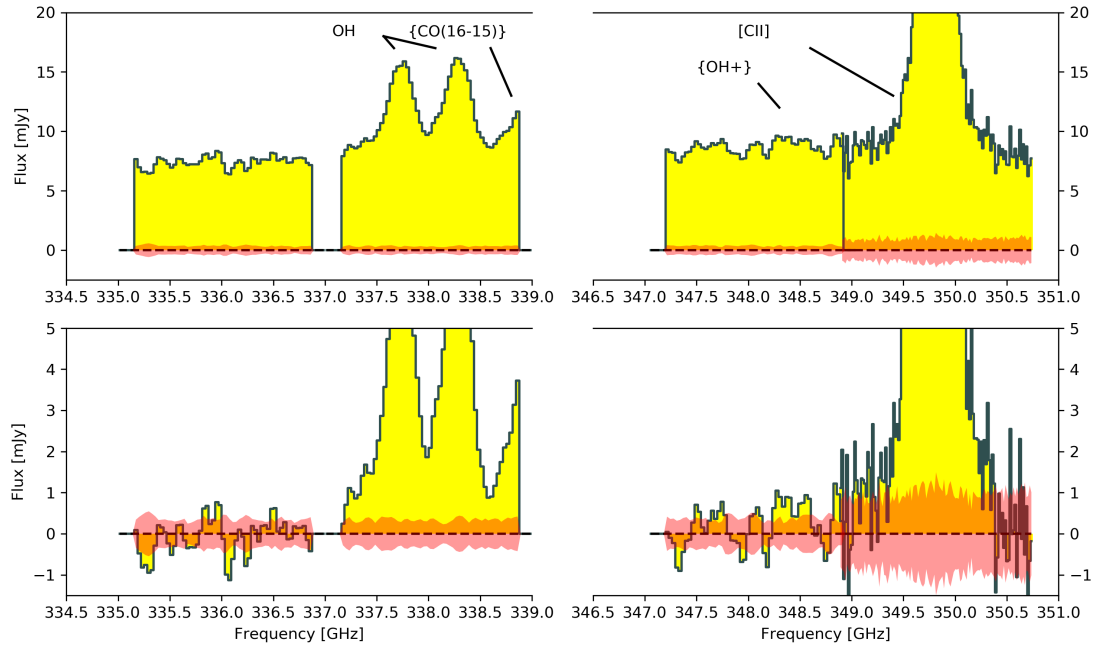


**Fig. A.2.** Pre-continuum-subtracted (top) and post-continuum-subtracted (bottom) spectra of BRI0952 extracted from the same region as the spectra (black circle shown in panel 1 of Figure 2 using a fit on the order of 1 and encompassing frequency ranges from  $\sim 335.3 - 336.9$ ,  $347.1 - 347.7$ ,  $348.97 - 348.98$ , and  $350.45 - 350.67$  GHz. The red region represents the  $1\sigma$  rms of the image. We do not show the atmospheric transmission as there are no relevant features in the frequency range. We note that the spectral window of the [C II] line has a higher noise level per channel compared to other spectral windows.



## Appendix B: Lensing model for BRI0952

This appendix includes the figures detailing the VISILENS lensing model results, which are given in Fig. B.1.

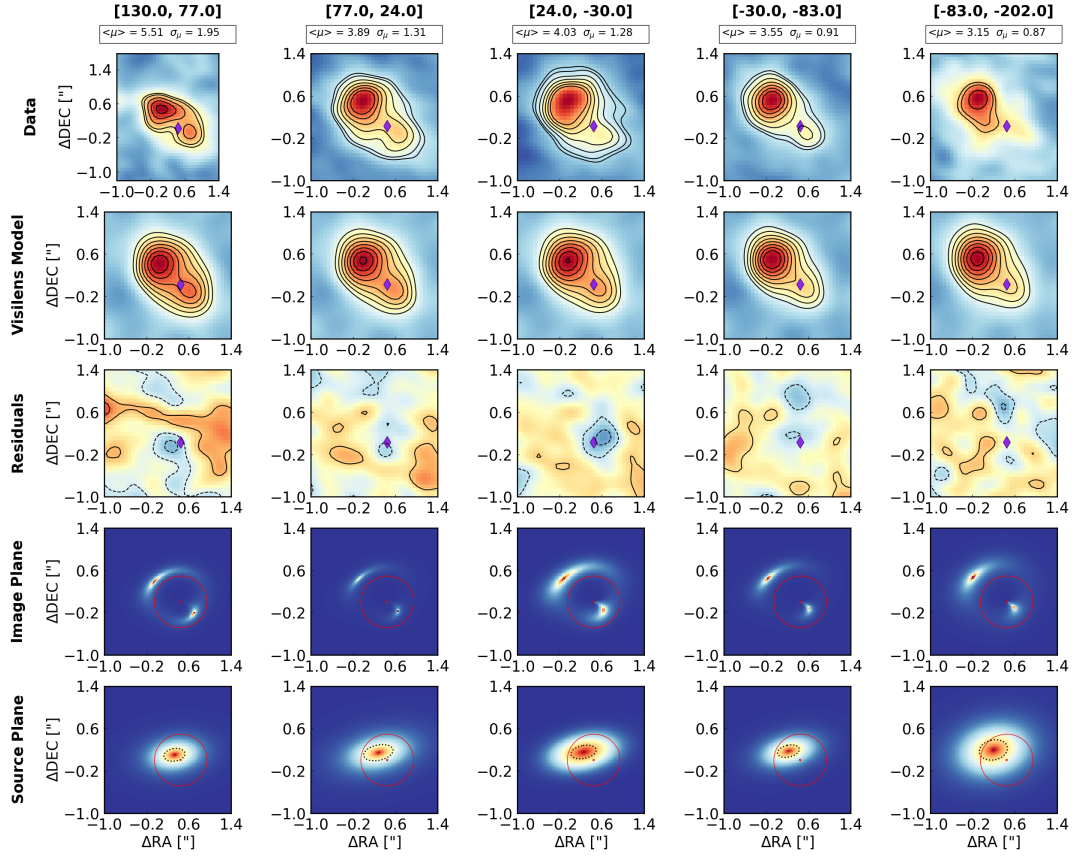


**Fig. B.1.** Image and lens models for BRI0952 for the velocity range shown at the top of each row. The diamond in the first three rows shows the best-fit position of the lens. Panels from top to bottom: Row 1 shows the ALMA band-7 dirty image with contours at 4, 6, 8, 10, 12, 14, and 16  $\sigma$  levels and the magnification value found for that bin; row 2 shows the image plane model from VISILENS with the same contour levels as row 1; row 3 shows the residuals after the subtraction of the VISILENS model, and contours are at -3, -2, -1, 1, and 2  $\sigma$  levels; row 4 shows the image plane model from VISILENS, and the red circle and point represent the critical and caustic lines; row 5 shows the source plane model with the black dashed ellipse showing the position of the source. All images are centered around the ALMA phase center (the (0.0, 0.0) coordinate in this case; see Table 3).

### Appendix C: Lensing model for companions to BRI0952

Appendix includes the figures detailing the VISILENS lensing model results for the companions of BRI0952, which are given in Fig. C.1.

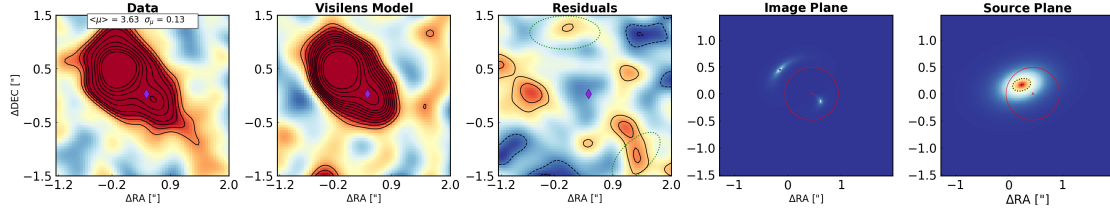


**Fig. C.1.** Image and lens models for BRI0952 isolated to the velocity range in which Comp-N and Comp-SW manifest. The diamond in the first three rows shows the best-fit position of the lens. Panels from top to bottom: Row 1 shows the ALMA band-7 dirty image with contours at 3, 4, 5, 6, 8, 10, 12, 14, and 16  $\sigma$  levels and the magnification value found for that bin; row 2 shows the image plane model from VISILENS with the same contour levels as row 1 and the residuals after the subtraction of the VISILENS model, contours are at -3, -2, 2, and 3  $\sigma$  levels; row 4 shows the image plane model from VISILENS, and the red circle and point represent the critical and caustic lines; row 5 shows the source plane model with the black dashed ellipse showing the position of the source. All images are centered around the ALMA phase center (the (0.0, 0.0) coordinate in this case; see Table 3).

### Appendix D: BRI0952 Img-N [C II] spectra

Appendix includes the [C II] spectra from Img-N of the quasar BRI0952 used in analysis of outflow properties as described in Section 4.5.

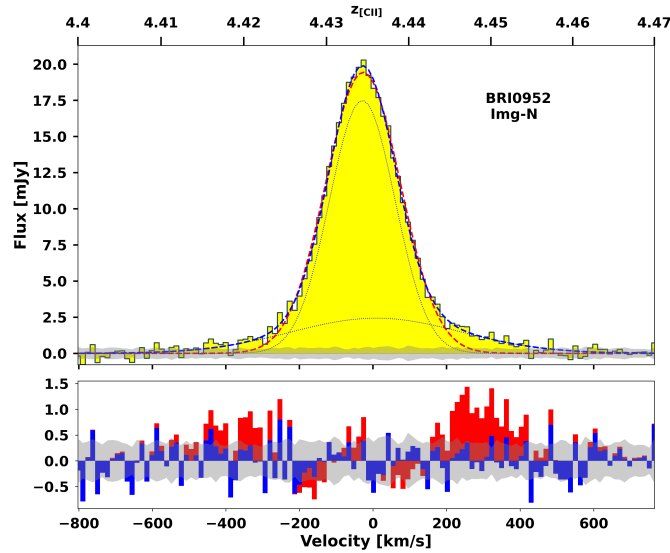


**Fig. D.1.** [C II] spectra extracted from Img-N of the quasar BRI0952. The single Gaussian is plotted in red, whereas the double-Gaussian fit to the line is plotted in blue. The wings are clearly visible, from which the outflow rate was calculated when investigating the effect of differential magnification described in Section 4.5.

### Appendix E: Velocity gradient of LBG-3

This appendix includes a velocity map showing the velocity gradient detected in [C II] between LBG-3 and AzTEC-3.

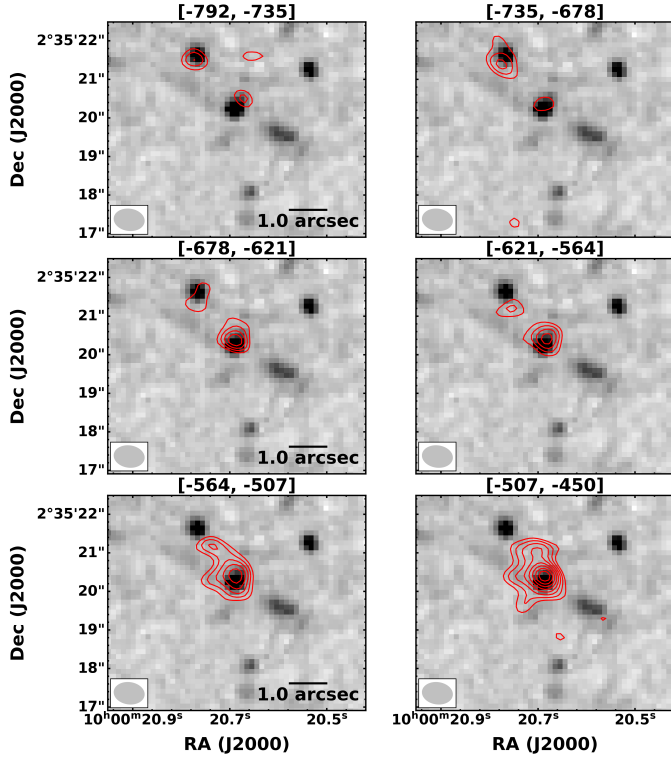


**Fig. E.1.** Velocity map of AzTEC-3 contours overlaid on *HST* F105W centered around the velocities at which the slight velocity gradient between LBG-3 and AzTEC-3 is visible. The velocity range is added to the top of the images. The red contours are at 3, 4, 5, 6, 7, 8, 9, and 10  $\sigma$  levels.

### Appendix F: [C II] and continuum offset of LBG-3

This appendix includes figures showing the [C II] and continuum offset for LBG-3.

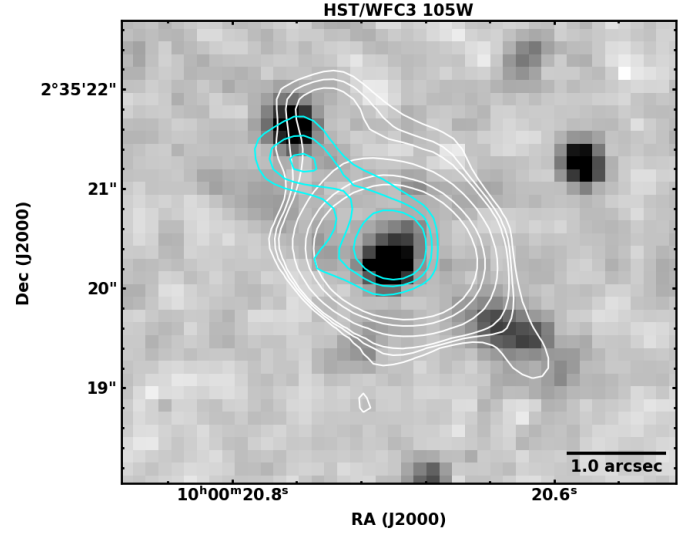


**Fig. F.1.** *HST* image of AzTEC-3 system with overlaid contours from the [C II] emission for LBG-3 (cyan) and continuum contours (white). The [C II] contours are shown at 3, 4, 5, and 6  $\sigma$  levels and 3, 4, 5, 6, 10, 20, and 30  $\sigma$  levels for the continuum.